International Journal of Biological Macromolecules 246 (2023) 125659

Contents lists available at ScienceDirect

International Journal of Biological Macromolecules

journal homepage: www.elsevier.com/locate/ijbiomac

Structural and mechanical analysis on mannuronate-rich alginate gels and xerogels beads based on Calcium, Copper and Zinc as crosslinkers

Belen Reig-Vano [a], Cristian Huck-Iriart [b], Silvia de la Flor [c], Anna Trojanowska [a], Bartosz Tylkowski [d], Marta Giamberini [a,*]

[a] Department of Chemical Engineering, Universitat Rovira I Virgili, Av. Països Catalans, 26, 43007 Tarragona, Spain
[b] ALBA SYNCHROTRON LIGHT SOURCE, Carrer de la Llum 2-26, 08290 Cerdanyola del Vallès, Barcelona, Spain
[c] Department of Mechanical Engineering, Universitat Rovira I Virgili, Av. Països Catalans, 26, 43007 Tarragona, Spain
[d] Eurecat, Centre Tecnològic de Catalunya, Marcel·lí Domingo s/n, 43007 Tarragona, Spain

ARTICLE INFO

Keywords:
Alginate gel
Encapsulation
Cation-crosslinking

ABSTRACT

Beads based on a mannuronate(M)-rich alginate (86 % M units) were prepared by adding the polysaccharide solution to a crosslinking bath containing different concentrations (0.5, 2 and 10 wt%) of XCl_2 where X = Ca, Cu or Zn. Primarily focus was on Zn, due to its antioxidant, anti-inflammatory and anti-microbial capabilities. The beads were characterized by Field-Emission Scanning Electron Microscopy (FESEM), Fourier-Transform Infra-Red spectroscopy (FT-IR), Thermogravimetric Analysis (TGA), Small-Angle X-ray Scattering (SAXS) and compression tests. The crosslinking agent significantly influenced the properties of the resulting beads. Specifically, Ca-based beads exhibited a smoother surface, while Cu- and Zn-based beads appeared rougher. Interestingly, Zn-based beads displayed a core-shell structure. Young moduli ranged from 3500 and 7000 MPa, with the highest values observed for Zn-beads. SAXS investigation at 0.5 wt% XCl_2 suggested increase in the densely packed domains amount in the order: Ca < Cu < Zn. Extended X-ray Absorption Fine Structure (EXAFS) showed that the coordination number was 4.3 ± 0.4 for Cu, and 4.0 ± 0.2 and 1.1 ± 0.1 for Zn in 0.5 wt% XCl_2 alginate xerogels, in agreement with reported Density Functional Calculations on Cu^{2+}– and Zn^{2+}–MM complexes. The results from FT-IR, compositional analysis and EXAFS collectively suggested a bridging coordination for these systems.

1. Introduction

Alginates are a family of linear polysaccharides which consist of β(1 → 4) linked β-D-mannuronic acid (M) monomers and its C-5 epimer α-L-guluronic acid (G) [1,2] (Fig. 1). Uronates may be arranged as homosequences of consecutive M or G residues (M- or G-blocks) alternating with G/M heterosequences (GM-blocks) [2–4]. Alginates are mostly derived from various species of marine brown algae. The distribution of block depends not only on the algae species, but also on factors such as age, harvested part and the seasonal variation [5]. Despite being obtained from the same algae and having similar composition, alginates can exhibit variations in their molecular weight distributions [6].

Among biopolymers, the application of alginate is relevant due to its biocompatibility, biodegradability, relatively easy obtention and the capacity to form hydrogels [3]. Alginate hydrogels and its derivates have found applications in diverse fields including cosmetics, food (as a stabilizer, gelling agent and emulsifier) [7–9], biomedical and pharmaceutical industry [10], as well as in medicine and biotechnology - for imaging and diagnosis tools, scaffolds for tissue engineering, biosensing [11], drug delivery systems [12] and cell encapsulation [13] and transplantation [14]. Most applications of alginate-derived hydrogels are possible because gelation happens under mild conditions.

Alginate gelation can be achieved through ionotropic gelation or acid precipitation [8]. Ionotropic gelation occurs when a polymeric solution of alginate is dropped into a solution of polyvalent cations. Consequently, crosslinking occurs, resulting in the formation of hydrogel beads and interactions evolve during the so called “maturation time”. The interaction between the crosslinking cations and alginate chains has been commonly described by the “egg-box” model, which suggests that negatively charged alginate chains – particularly G-blocks – form electronegative cavities capable of hosting cations [1,15,16]. Although only G-blocks were initially believed to be responsible for

* Corresponding author.
E-mail address: marta.giamberini@urv.cat (M. Giamberini).

https://doi.org/10.1016/j.ijbiomac.2023.125659
Received 2 May 2023; Received in revised form 22 June 2023; Accepted 30 June 2023
Available online 3 July 2023

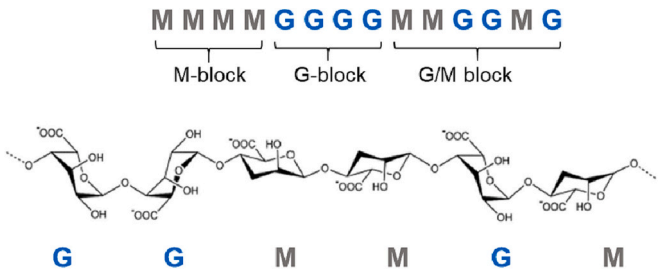

Fig. 1. Chemical structure of alginate.

intermolecular crosslinking [3], MGM-blocks may also contribute through weak interactions [1,17,18]. The physicochemical properties of hydrogels are influenced not only by the composition and molecular weight (Mw) distribution but also by the properties of the ions involved, such as valence and radius. Eventually, the affinity of multivalent cations employed as crosslinking cations can be ranked as follows: Mn < Zn, Ni, Co < Fe < Ca < Sr < Ba < Cd < Cu < Pb [8].

The pKa values of M and G residues are 3.38 and 3.65, respectively [8]. Therefore, carboxyl groups are deprotonated over a wide range of pH values. Higher pH values induce repulsion between the polymeric chains, which are strongly hydrophilic. However, pH values below the pKa result in protonation of carboxyl groups, causing aggregation of alginate chains and acid precipitation [8,19].

Understanding the gelation process and its impact on the physicochemical properties of alginate hydrogels has been the subject of numerous investigations. Such studies are significant for several reasons. Firstly, understanding the factors influencing gelation, such as the crosslinker type and concentration, and the pH of the crosslinking bath, enables the control of the properties of the resulting gels, which could be tailored for specific applications in the food, pharmaceutical, and biomedical industries. Furthermore, by totally comprehending the gelation system and the effects of each factor, a more efficient and fruitful production could be achieved. Therefore, the study of alginate gelation and crosslinking interactions is crucial, not only for regulation but also for prediction of the physicochemical features of the resultant alginate hydrogels, ensuring consistent quality and safety. For instance, the characteristics of alginate hydrogels are directly related to safety in drug delivery systems: the performance of hydrogels under certain conditions determines not only the encapsulation efficiency of therapeutic compound but also targeted action, controlled delivery and rate and, therapeutic dose.

Similarly, in tissue engineering, predicting and tuning the characteristics of alginate gels such as degradation rate and assistance to cell growth support the success of the therapy. The estimation of these features can avert treatment failures while medical therapies can be upgraded. In addition, the prediction of hydrogels properties can promote the development of novel strategies and unique structures that behave efficiently under specific conditions. Moreover, properties such as strength, targeted activity and ductility of current alginate-based materials can be ameliorated by understanding the factors involved in their modification. Therefore, apart from improving existing materials, new ones can be manufactured in order to develop not only enhanced but also original and innovative products.

The purpose of the present paper is to study the interactions between alginate residues and different cations in detail and obtain quantitative information of the binding amount and nature of these interactions. To the best of our knowledge, the potential applications of gels based on high-M content alginate have not been widely explored. Indeed, high-M alginates, due to their lower viscosity, can be used to prepare gels with higher stability and low permeability, providing efficient protection to immobilized cells [20]; it has been also shown that high-M alginates give rise to emulsions with stable and fine droplets [21], which is very important in micro- and nanoencapsulation technologies. The G/M ratio has also shown to be an important factor in controlling the radical scavenging activity of alginate, being more pronounced when M content is high [22]. High-M alginates have also demonstrated as very good candidate as nanocarrier of oral insulin [23]. The reason for the scarce studies regarding to high-M alginates would be the limited availability of high-M alginates in nature [24]. Indeed, these kinds of alginates are often produced by chemical or enzymatic modification of natural alginates, which supposes a higher production cost [25]. Nevertheless, this kind of production assures the obtainment of high quality alginates with well-defined properties, which make them suitable for high-value applications such as medical field. Moreover, the mostly accepted "egg-box" model for alginate gels predicts a selective binding of the divalent cations to the guluronate units at low metal concentration [26]. As a result, despite their great potential, the properties of hydrogels based on high-M alginates have not been thoroughly studied and their applications are still unusual.

Huge amount of literature exist on this general topic, especially focused on Ca- or Cu-alginate gels, prepared out of several ranges of cation concentrations and maturation times [3,27–32]. Actually, in the literature we could not find any systematic investigation addressing the optimization of maturation time, which was reported to range from 30 min to several hours without clear justification of its selection. Consequently, it is challenging to get insight into the factors that may affect the final characteristics of the resulting beads, provided that a comparison between different studies would not be rigorous.

We hypothesized whether the crosslinking mechanism of each cation could be correlated with the physico-chemical properties of the obtained hydrogels, specifically concerning the M fraction of the employed alginate. Given that diversification of crosslinkers is the main source of materials with different features, calcium (Ca^{2+}), copper (Cu^{2+}) and zinc (Zn^{2+}) chlorides were employed as crosslinking agents at different concentrations – 0.5 %, 2 % and 10 % wt%.

Zn^{2+} was of particular interest due to the limited knowledge of alginate crosslinking mechanism involving this cation. $Zn^{2+}$is an essential element in our organism, since it plays a role in numerous cellular processes, including cell growth, differentiation and wound healing. Additionally, zinc has demonstrated antioxidant, anti-inflammatory and anti-microbial capabilities [33]. Furthermore, Zn^{2+} is widely available and sustainable, what makes it a sustainable choice for medical devices [34,35]. Indeed, Zn-based hydrogels evidenced potentially valuable properties for future purposes as delivery systems or enhancement of wound healing process [36]. Since Zn is a soft metal, its ions form coordinative covalent-like bonds with the alginate carboxylates, which results in stronger and more stable hydrogels, compared to Ca^{2+}, and allows better fine-tuning of drug release [37,38]. Nevertheless, Zn^{2+} has not been extensively employed for studies of alginate gelation compared to Ca^{2+} and Cu^{2+}, as far as we found in bibliography. In contrast, Zn^{2+} interaction with alginate is known to be less specific than with Cu^{2+}; however, the weaker affinity of alginate for Zn^{2+} could be considered an advantage as the crosslinking mechanism could be tuned easier, possibly enabling the formation of more complex structures. On the other hand, copper alginate hydrogels showed cytotoxicity to mammalian cells, which limit their use despite their excellent antibacterial properties [39]. Nevertheless, extensive research has been conducted on alginate hydrogels based on complexation with copper, particularly due to their strong coordination and potential applications in agriculture and environmental protection [40,41]. These studies represent a useful reference in the investigation of transition metals-alginate complexes.

Therefore, in this paper we focused on investigating aspects of high-M alginate beads preparation:

- Firstly, beads' maturation was monitored through FT-IR, morphological and microscopic analyses. Based on these analyses, a maturation time of 48 h was selected for all the subsequent experiments in order to get comparable systems.

- Secondly, the study aimed to explore the differences in gelation behavior between Ca, Cu and Zn as crosslinkers with alginate. The diverse gelation mechanisms and conditions, including the influence of the pH, cation species and concentration – and the physico-chemical properties of the obtained hydrogels were related in terms of morphology, interactions involved, nanoscale structure and mechanical properties. Notably, our analyses were all performed on xerogels, in contrast to previous literature reports that focused on aerogels. In particular, the use of Zn as a crosslinker was explored, which has not been widely considered in the literature.
- Lastly, further understanding of the coordination mechanism was attempted when alginates with high-M content are employed, since most existing studies in the literature primarily focus on low and medium-M alginates. By investigating the properties of high-M content alginates, the aim is to propose wider applications for these materials based on their unique properties.

2. Materials and methods

2.1. Materials

Sodium alginate and hydrochloric acid (37 %, ACS) were by supplied by PanReac AppliChem. Calcium chloride anhydrous (Granular, <7.0 mm, >93.0 %), zinc chloride (reagent grade, >98 %) and deuterium oxide were acquired by Sigma-Aldrich. Copper (II) chloride dihydrated (reagent grade, >98 %) was purchased from Fisher scientific. MilliQ water was produced in our laboratory.

2.2. Methods

2.2.1. Preparation of alginate beads

Calcium, copper and zinc (Ca-, Cu- and Zn-) beads were produced by external ionotropic gelation. Briefly, hydrogels were prepared by dropping 10 g of polymeric solution of sodium alginate 1.7 % (*w*/w) into 200 g of aqueous solutions XCl_2, where X represents Ca, Cu or Zn. The concentrations of XCl_2 used were 0.5, 2 and 10 (wt%). The extrusion was performed using a peristaltic pump (KDS 100 LEGACY SYRINGE PUMP, KDScientific) and an extrusion rate of 0.4 mL/min. The resulting beads were left under stirring (100 rpm) for 48 h into the cation solution. The beads were collected by filtration, washed with distilled water and dried in an oven at 40 °C. After 24 h, they were stored in transparent flasks for further studies.

2.2.2. Microscopic observation

The dimensional distribution and morphology of wet beads at various maturation times (1, 6, 24 and 48 h) was investigated using an optical microscope (LEICA DM 2500, Leica microsystems, Wetzlar, Germany). The projection diameter of wet beads was determined through image analysis using publicly available software (Image J software, Wayne Rasband, National Institute of Health, Bethesda, MD, USA). Particle size was calculated as the average value obtained from analyzing at least 10 beads for each concentration and for the three different crosslinking cations.

2.2.3. ^1H nuclear magnetic resonance (NMR)

The ^1H NMR spectra of the sodium alginate solutions in D_2O were recorded on the spectrometer Varian Gemini 400 MHz (^1H Proton Larmor frequency of – 400 MHz, Bruker Corporation, Billerica, MA, USA) at 70 °C with a pulse delay time of 5 s. Presaturation was applied during the relaxation delay and mixing time with 25 Hz (sample 1) and 10 Hz (sample 2). Hence, 20 mg of sodium alginate were dissolved in 1 mL of D_2O. Previously reported sodium alginate ^1H NMR spectra were taken as a reference for the assessment of our samples.

2.2.4. Environmental scanning electron microscopy (ESEM)

A morphological analysis of the hydrogels' surface and cross-section was carried out by Environmental Scanning Electron Microscopy (ESEM) in a FEI ESEM Quanta 600 instrument (Netherlands). Dry samples were fixed to metal stubs with two-sided adhesive carbon tape. For cross-sections, dry beads were previously frozen with liquid nitrogen and cut using a surgical blade.

2.2.5. Cryofracture

Some beads were cryo-fractured with liquid nitrogen. Hence, samples were taken during maturation time at: 1 h, 6 h, 24 h and 48 h. Cryogenic procedure was performed in a cryopreparation system Epredia cryostat, CryoStar NX50 (Fisher Scientific, Waltham, Massachusetts, USA). Free-break surfaces were obtained, fixed to metal stubs with carbon tape and coated with a gold layer (30 mA, 3 min, 5 kV, 50 pA) using an ion sputter SCD 040 (Bal-Tec, Balzers, Liechtenstein). Afterwards, samples were examined by ESEM.

2.2.6. Attenuated total reflectance Fourier transform infrared (ATR-FT-IR) spectroscopy

Attenuated total reflectance Fourier transform infrared (ATR-FT-IR) absorbance spectra of the dry beads were obtained within 400 to 4000 cm^{-1} wavenumber range with 4 cm^{-1} resolution using a spectrometer 680 Plus (Jasco Analitica Spain, Madrid, Spain). All spectra were recorded and baseline corrected and smoothed using OPUS software. For maturation time determination, beads were withdrawn at different times from the coagulation bath, dried as previously described and analyzed.

2.2.7. Thermogravimetric analysis

Thermogravimetric analyses (TGA) were performed in Mettler-Toledo TGA/SDTA 851e thermobalance (Mettler-Toledo Inc., Schwerzenbach, Switzerland) under oxygen flow (50 mL/min). Samples were heated from 30 to 800 °C at 10 °C/min. In each test, 18 mg of each sample were used. Analysis started after holding isothermally at 30 °C for 15 min.

2.2.8. Wide Angle XRD (WAXS)

The composition of TGA residues and the packing of dry X-alginate beads were characterized by wide angle X-ray diffraction (WAXS), using a diffractometer D8-Advance (Bruker-AXS, Billerica, Massachusetts, USA). Cuk_α radiation was obtained from a copper X-ray tube operated at 40 kV and 40 mA. Diffracted X-rays were detected with a PSD detector LynxEye-XE-T. The diffractograms were recorded and read with the software DIFFRAC.EVA 5.2 from Bruker.axs and the database PDF-2 release 2018 from ICDD (International Center for Diffraction Data). In the case of alginate beads, they were mechanically pulverized before performing the test.

2.2.9. Compression tests

The mechanical properties in compression were evaluated using a dynamic-mechanical thermal analyzer DMAQ800 (TA Instruments, New Castle, DE) in static mode and using the compression clamp (15 mm diameter plate). Compression strength was evaluated at 25 °C with a ramp force of 2 N/min. The diameter (D) of each capsule was measured using a Mitutoyo 547 digital Thickness Gage for precise measurements (resolution 0.01 mm, accuracy ±20 μm). To evaluate the failure behavior of each capsule, photographs before and after the compression test were taken with a Digital Microscope Leica DMS1000 (Leica, Wetzlar, GE). At least ten beads of each material were tested, and the statistical results were reported.

The force (F) versus displacement (ΔL) curve was obtained for each capsule. To evaluate the stress at break (in case of broken beads), it was assumed that the contact surface was the transverse circular section:

$$\sigma_{break} = \frac{F_{break}}{\frac{\pi}{4} \cdot D^2} \quad (1)$$

Young's modulus was obtained from the linear part of the curve F-

$(\Delta L/2)^{3/2}$ using Hertz Theory [42] and assuming a Poisson ratio of 0.5 [43,44].

$$F = \frac{4}{3} \cdot D^{0.5} \frac{E}{1-\nu^2} \left(\frac{\Delta L}{2}\right)^{\frac{3}{2}} \tag{2}$$

2.2.10. Small Angle X-ray Scattering (SAXS)

2.2.10.1. Methods. Small Angle X-ray Scattering (SAXS) measurements were performed in the BL11 NCD-SWEET beamline from the ALBA Synchrotron Light source, Barcelona, Spain (project ID 2022097172). Metal-alginate xerogel beads were placed between Kapton tape. The incoming beam energy was set at 15 keV with a sample detector distance of 3600 mm. 2D patterns were recorded in a Pilatus 1 M (Dectris, Switzerland) detector. Patterns were recorded during 1 and 30 s integration, where no radiation damage effects were observed during measurements. Isotropic 2D patterns were integrated using pyFAI library [45] where the obtained q-range was between 0.07 and 3.5 nm-1 where $q = (4\pi/\lambda)sin(\theta)$ with λ incoming beam wavelength and 2θ the scattering angle.

2.2.10.2. SAXS models. After drying/aging the beads evolve to compact structures where part of the beam showed some degree of low periodic order but densely packed domains. The formation of small crystalline structures affected the low angle region with the appearance of a power Law of ca. 4 (smooth surface crystals) and a clear diffraction peak between 1.4 and 1.65 nm^{-1} depending on the sample (4.5–3.8 nm expressed in $d_{spacing} = 2\pi/q$). However, part of the remaining original structure obtained from the hydrogel could be observed.

Previews reports in Alginate based hydrogels showed a rod-like structure [46], thus, we approximated this object thought a semi-empirical Guinier-Porod function [47] which is given by a split function which contains a Guinier and a Porod function:

$$GP\left(q, R_g, s, d\right) = \begin{cases} \frac{1}{q^s} exp\left(-\frac{R_g^2 q^2}{3-s}\right) \; if \; q \le Q_1 \\ \frac{D}{q^d} \; if \; q \ge Q_1 \end{cases} \tag{3}$$

where D is calculated such that the Guinier and the Porod function presents continuity at the boundary point Q_1 as its first derivative. Here, "R_g" is the radius of gyration of the scatterer, "s" the power law exponent at low angles (fixed at 1 for rod-like structures) and "d" the Porod exponent. The "s" parameter was fixed due to the presence of larger compact structures which contributed to the registered scattered intensity. The Q_1 value is:

$$Q_1 = \frac{1}{R_g}\left[\frac{(d-s)(3-s)}{s}\right]^{\frac{1}{2}} \tag{4}$$

In the present data, a Porod exponent of 4 (smooth surface) was observed. This exponent corresponds with the power law at medium regimes described by other authors (usually called α_2) [2,4,5] however, exponents near 4 were observed in low pH hydrogels [48], moreover, it is expected that the drying process made the structure more compact, hence, this parameter was kept fixed in order to decrease the number of fitting variables. The final model considered a rod-like structure and diffraction contributions considering a Gaussian profile (Eq. (5)):

$$\begin{aligned} I(q) = {} & C_1 P_{GP}(q, Rg) + C_2 G(q, qc_1, FWHM_1) + \\ & + C_3 G(q, qc_2, FWHM_2) + C_3/q^p \end{aligned} \tag{5}$$

C_1, C_2,C_3, C_4 are scalars, qc_1 and $FWHM_1$ are the position and width of a Gaussian function for the diffraction peak: qc_2 and $FWHM_2$ are the position and width of the amorphous material (background at high angles) and finally the parameter p is the power law function for the background at very low angles (ca 4). Patterns were analyzed using an *in-house* written program in Python 3.8 using the lmfit library for least-square procedures.

2.2.10.3. EXAFS analysis. Extended X-ray absorption fine structure (EXAFS) measurements were performed at the BL16-NOTOS beamline at ALBA synchrotron Light Source in Barcelona, Spain (project ID 2021025034). The EXAFS spectra of the Cu, Zn k-edges were recorded at room temperature in transmission mode with three ion chambers as detectors with gas mixture optimized to improve the measured signal. Third ionization chamber was used to measure the Cu and Zn metallic references simultaneously with the sample for energy calibration. The samples were placed between Kapton windows. The EXAFS data were extracted from the measured absorption spectra by standard methods using the LARCH software, which is part of the IFFEFIT package. The structural parameters (coordination numbers, bond lengths, and their mean squared disorders) were obtained by a nonlinear least-squares fit of the EXAFS signal in R-space. The theoretical scattering path amplitudes and phase shifts for all the paths used in the fits were calculated using the FEFF code.24 The k-range was set from 3 to 14 $Å^{-1}$ and the Fourier transforms were fitted in different regions. The passive reduction factor S0 was restrained to a value of 0.90 for Zn and 0.88 for Cu. This value was obtained from fitting the EXAFS spectrum of a metallic Zn and Cu foils respectively and by constraining the coordination number of each metallic component.

3. Results and discussion

3.1. Alginate characterization

The gelation mechanism of alginate in the presence of divalent cations has been generally explained in terms of the "egg-box" model [49]. According to this model, homosequences of guluronates form negatively charged cavities can easily host metal cations, while M-blocks or alternating M-G blocks exhibit lower affinity for the cations. Nevertheless, alternative structures have also been proposed according to X-ray diffraction and NMR studies [50,51]. On the other hand, density functional calculations performed on uronate dimers, showed that metal complexation cannot be clearly attributed to the presence of GG or MM blocks, particularly in the presence of an excess of ions [52]. In the literature, studies on alginate gels refer on materials with a broad range of M/G ratio, typically ranging from approximately 0.5 to 1.6, classified as High G (High-G) content and Low G (Low-G or High-M) content, respectively [29,53–55]. Therefore, it is of great importance to determine the composition of the alginate under investigation in order to establish correlations between its composition and the gelling, structural, and mechanical properties in the presence of the different considered cations. The M/G ratio was determined by ^1H NMR spectroscopy following the method described by Belattmania et al. [56].

Alginate spectra presented in Fig. 2 was recorded at 70 °C to reduce the viscosity of the analyzed sample, resulting in narrower line-widths of recorded spectra and improved spectral resolution. The resulted spectra showed the reported frequencies of mannuronic and guluronic acids contributions [57]. Three specific peaks were focused on for sequence determination within the sodium alginate polymeric chain: (I) the peak attributed to H-5 of guluronic acid residues in the homopolymeric G blocks at 4.5–4.6 ppm, (II) the overlapped peaks of anomeric hydrogens of mannuronic acids (M1) and the H-5 of alternating blocks (GM-5) at 4.6–5.3 ppm, and (III) the peak of anomeric hydrogen of guluronic acid residues (G) at 5.4–5.6 ppm. The areas of abovementioned peaks were used to calculate the M/G ratio, monad molar fractions (M and G), as well as diads sequences (MM, GG, GM, MG) by employing the formula given by Grasdalen et al. [58].

Remarkably high molar monad fractions M and diad fractions MM were registered. The monad molar fraction of M (FM) was found to be

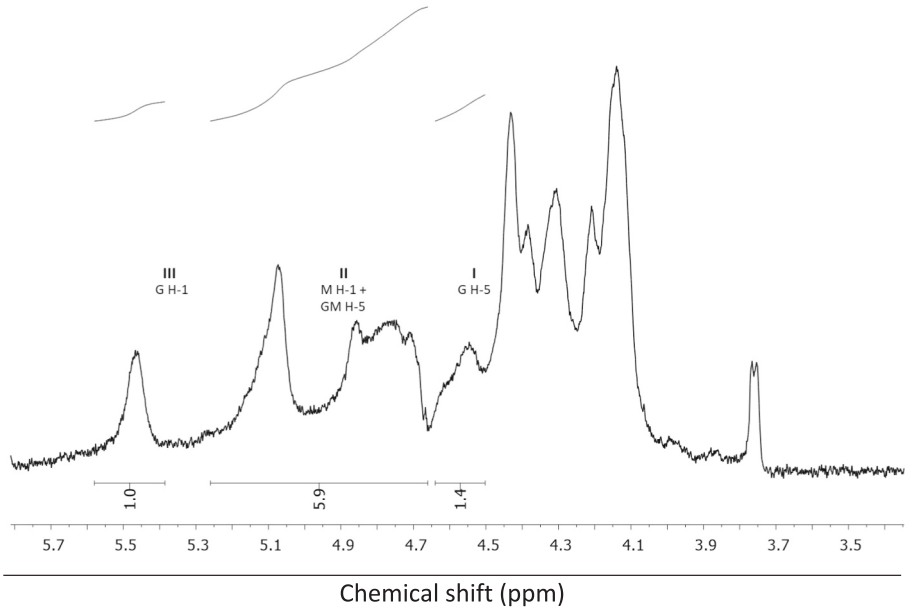

Fig. 2. ^{1}H *NMR spectra of* sodium alginate using D_2O as a solvent, recorded at 70 °C with the presaturation of 25 Hz applied during the relaxation delay and mixing time.

0.86, whereas for G (FG) it was 0.14. The diads fractions were as follows: FMM = 0.81; FGG = 0.19; FGM = 0.05. Based on these results, the calculated M/G ratio of the studied alginate gave an unprecedently high value of 6.08, indicating a significant predominance of MM blocks and classifying the analyzed alginate as Low-G or High-M content alginate. As mentioned earlier, the distribution of the M and G units greatly affect the gelling properties. According to the "egg-box" model, this extreme dominance of M units in studied alginate should drastically reduce ionic

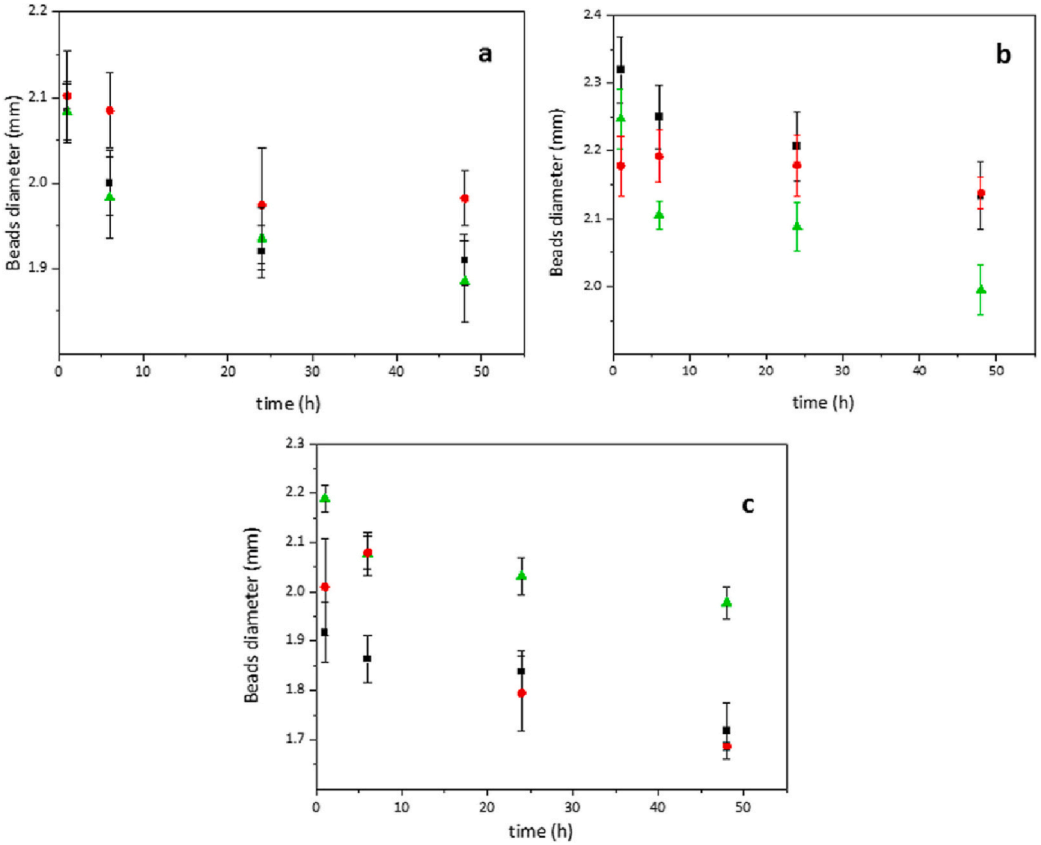

Fig. 3. Average beads' diameter versus maturation time for Ca-based (a), Cu-based (b) and Zn-based (c) alginate gels obtained from bath containing: (■) 0.5 %, (▲) 2 %, (●) 10 % metal chloride.

binding and create hydrogels with entangled network of relatively long and elastic M segments. Thus, the resulting gel is expected to be more dynamic and with higher porosity and permeability in comparison to hydrogels produced from HG content alginates [59].

Therefore, to explain the general behavior of the alginate under investigation, it is reasonable to assume that MM dimers are predominant over GM, MG or, more neglectable, GG. However, for simplicity, the saccharide units will be generally referred to as U (uronate).

3.2. Preparation of alginate beads

Ionic gels were prepared as described in the experimental part. Optical Microscopy images of all the obtained beads are shown in Fig. S1-S3. Upon extrusion of the polymeric solution into the crosslinking solution containing divalent cations, immediate bead formation takes place. Afterwards, beads density progressively increases during the maturation process, which is influenced by factors such as the type and concentration of the cation used, pH and ionic strength [31,60]. In this work, the maturation step of the alginate beads was done during 48 h, which was notably longer than most studies reported in the literature, where it generally lies between 3 and 24 h. However, it must be considered that the evolution of these systems is quite slow, since the crosslinking reactions that determine gel formation proceed from the outer to the inner part of the beads, accompanied by syneresis. Therefore, it was expected to require longer times to reach steady-state equilibrium conditions, especially in the presence of high amount of cation.

In order to establish the maturation time, we monitored wet beads' diameter over time during the crosslinking process. Results are shown in Fig. 3. for the range 1–48 h.

In general, the beads' diameter decreased upon maturation, as expected due to syneresis: the solvent is expelled from the gel, which shrinks. After 48 h, a stable dimensional situation was apparently reached, since no significant variation in beads' diameters could be observed beyond this time point.

Additionally, in order to confirm the adequacy of a 48-h maturation period for the development of beads, we conducted additional experiments using FT-IR analysis at different maturation time intervals.

In the literature, previous research has employed FT-IR to investigate the coordination characteristics of metal-alginate complexes, through the evaluation of the differences ($\Delta\nu$) between the asymmetric and symmetric vibrational modes of carboxylate groups in the formed beads [55,61]. The comparison between the $\Delta\nu$ values of the ionically-crosslinked alginate and those of the uncrosslinked sodium alginate should provide information regarding the nature of metal coordination. Therefore, $\Delta\nu$ could serve as a probe of beads' maturation, whereby reaching a constant $\Delta\nu$ value implies the establishment of a stable coordination within the beads and an adequate maturation time.

As a matter of example, Fig. 4 reports the FT-IR spectrum ranging from 600 to 4000 cm^{-1} of Ca-, Cu- and Zn-alginate beads obtained from a XCl_2 0.5 wt% solution after 48 h maturation. The spectrum of Na-alginate is also included for comparison. In addition, Table 1 reports the $\Delta\nu$ values obtained at different maturation times for the different cations at the lowest (0.5 wt%) and highest (10 wt%) XCl_2 concentration in the coagulation bath. We focus our attention on the trends depicted in Table 1, while the final $\Delta\nu$ values obtained, together with Fig. 4, are further discussed in Section 3.7.

The values reported in Table 1 demonstrate that, in general, stable $\Delta\nu$ values were reached after 48 h maturation. The only exception is observed in the case of $ZnCl_2$ (at a concentration of) 0.5 wt%, where $\Delta\nu$ exhibits a very small variation and appears to stabilize after 24 h. However, in order to establish a standardized procedure, we selected 48 h as maturation time for all the investigated systems.

In this study, the properties of the obtained gels were examined by extruding the same amount of sodium alginate solution (1.7 wt%) into crosslinking baths containing 0.5, 2 and 10 wt% of X^{2+} chloride,

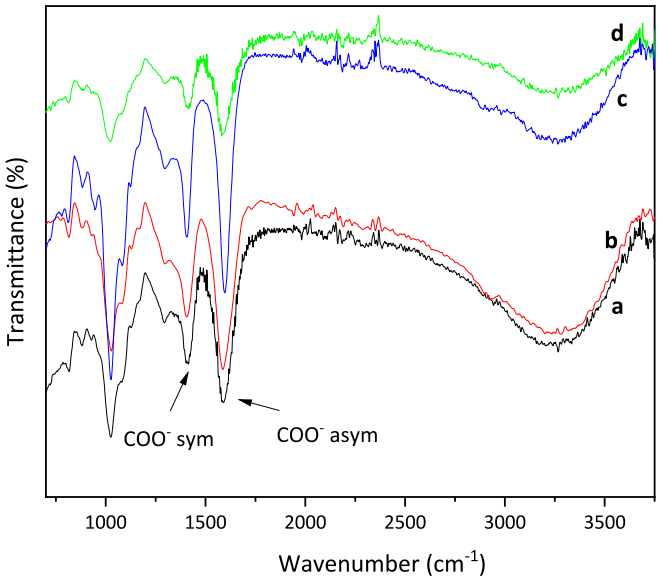

Fig. 4. FT-IR spectrum between 600 and 4000 cm^{-1} of Na-alginate, and of Ca-, Cu- and Zn-alginate beads obtained from XCl_2 0.5 wt% after 48 h maturation time. a) Zn; b) Cu; c) Na; d) Ca. Asymmetric and symmetric vibrational modes of carboxylate groups are highlighted.

Table 1
Differences $\Delta\nu$ between the asymmetric and symmetric vibrational modes of carboxylate groups of sodium alginate and alginate beads obtained from 0.5 wt % and 10 wt% XCl_2 (X = Ca, Cu and Zn) concentration at different maturation times.

Sample		Maturation time (h)			
		1	24	48	72
			$\Delta\nu$ (cm^{-1})		
Na alginate[a]	190		–	–	–
Ca beads ($CaCl_2$ 0.5 wt%)		174	174	165	165
Ca beads ($CaCl_2$ 10 wt%)		175	154	150	150
Cu beads ($CuCl_2$ 0.5 wt%)		170	174	180	180
Cu beads ($CuCl_2$ 10 wt%)		158	161	180	180
Zn beads ($ZnCl_2$ 0.5 wt%)		178	176	176	176
Zn beads ($ZnCl_2$ 10 wt%)		140	177	172	172

[a] Powder sample.

respectively. Therefore, in all cases, the gelification process occurred in the presence of a total cation amount higher than the theoretically needed amount to compensate for the exchange between Na^+ and X^{2+}, i.e. according to a ratio (X^{2+}/ Na^+) > 0.5. However, it is important to note that the different concentrations of X^{2+} result in varying pH values of the crosslinking baths, which are reported in Table 2.

Table 2
Values of pH as determined in the crosslinking baths containing different concentrations of Ca^{2+}, Cu^{2+} and Zn^{2+}; number of uronate units per cation ($n_{U/X}$) and of water molecules per cation ($n_{W/X}$) in the corresponding beads.

Cation X	Crosslinking bath concentration of XCl_2 (wt%)	XCl_2 concentration (mol/L)	pH	$n_{U/X}$	$n_{W/X}$
Ca^{2+}	0.5	0.045	7.89	2	4.4
	2	0.18	7.99	1.2	1.8
	10	0.98	10.31	1.3	3.4
Cu^{2+}	0.5	0.029	4.49	2	2.9
	2	0.12	4.1	2	3.9
	10	0.58	2.98	2.3	2.1
Zn^{2+}	0.5	0.037	6.93	2	4.5
	2	0.15	6.32	2	2.6
	10	0.80	5.31	2	2.7

These pH values can be interpreted based on the different reactions that take place between the cation and water [62]. Indeed, when $CaCl_2$ is employed as crosslinking agent:

$$Ca^{2+} + H_2O \leftrightarrows CaOH^+ + H^+ \; k = 10^{-12.6} \quad (6)$$

$$H^+ + Cl^- \rightarrow HCl\,(g) \; k = 10^{7} \quad (7)$$

The combination of (6) and (7) leads to an increase of $[OH^-]$ concentration, shifting the pH toward alkaline values. Considering the pK_a of alginic acid, which is approximately 3.4 [63] it can be observed that the pH of the crosslinking bath is higher than the pK_a of alginate for all investigated $CaCl_2$ concentrations. Therefore, only ionotropic gelation is expected to occur in this case.

On the other hand, when $CuCl_2$ is employed as cross linker, the strong Lewis acid character of Cu^2 leads to the following reactions:

$$Cu^{2+} + OH^- \rightarrow CuOH^+ \; k = 10^{6.3} \quad (8)$$

$$Cu^{2+} + 2OH^- \rightarrow Cu(OH)_2 \; k = 10^{12.8} \quad (9)$$

(8) and (9) determine an increase of $[H_3O^+]$ concentration and hence an acidic pH. In this case, in addition to ionotropic gelation, the precipitation of alginic acid was expected. In particular, the ratio [alginic acid]/[alginate] at 0.5 wt%, 2 wt% and 10 wt% $CuCl_2$ concentration is approximately 0.081, 0.20 and 2.6, respectively. This implies that at a 2 wt% $CuCl_2$ concentration in the crosslinking bath, the beads are formed as a hybrid system of copper alginate/alginic acid, while at 10 wt% $CuCl_2$, the precipitation of alginic acid may be predominant.

-Analogous reactions to (8) and (9) occur when $ZnCl_2$ is employed in the crosslinking bath. Nevertheless, in this case, the resulting pH of the bath is slightly acidic because Zn^{2+} is a milder Lewis-acid [64]. Hence, even in the most concentrated of Zn^{2+} solution (10 wt%), the ratio [alginic acid]/[alginate] is 0.012. Therefore, ionotropic gelation is predominant.

3.3. Structure of alginate beads

When the sodium alginate solution is dropped into the XCl_2 solution, beads are formed instantly, if the combination of concentration and intrinsic viscosity of the polysaccharide solution is above (surpasses?) a threshold value, which depends on the specific cation used [29]. Indeed, beads formation is contingent upon the integrity of the droplets when they meet the cation solution, with the entanglements of the polymeric chains playing a crucial role in this process. In our study, the alginate solution, with an approximate concentration of 17 g/L and an apparent viscosity of 866 mPa·s, could produce stable beads with each cation (Ca^{2+}, Cu^{2+}, Zn^{2+}) at the lowest concentration used (0.5 wt%), which is in line with the trends reported in literature [29]. Subsequently, the beads undergo a maturation process wherein the evolution of the gel beads progresses from the surface toward the inner part of the beads. During this maturation step, the density of the beads increases, syneresis occurs, mechanical properties change and finally a steady state is reached. Maturation is a slow phenomenon that depends on the cation diffusion through the initially precipitated gel layers and consequently affects the final morphology and inner structure of the beads. For this reason, in order to investigate this process, the evolution of the beads obtained at different cation concentration was monitored using SEM over diverse time intervals.

Fig. 5 shows the ESEM images of the dry beads, obtained after dropwise addition of sodium alginate into a bath containing 0.5 wt% XCl_2, 48 h maturation and finally dried at 40 °C for 24 h.

In all cases, stable beads were formed; nevertheless, the difference in their outer morphology is remarkable. The Ca-crosslinked beads (Fig. 5a), exhibit a smooth and uniform surface, whereas the Cu-crosslinked beads (Fig. 5b) display extremely rough and irregular surfaces looking like the aggregation of microgels. This effect is even more pronounced for Zn-crosslinked beads (Fig. 5c). This difference can be attributed to variations in the crosslinking mechanism. When the outer surface of the alginate solution drop comes into contact with the cation solution, a stronger interaction is established between alginate and Cu^{2+} or Zn^{2+}, compared to Ca^{2+}. As a result, a rigid wall is formed around the beads, which impedes diffusion of Cu^{2+} and Zn^{2+} toward the center of the beads. Conversely, Ca^{2+} diffusion is expected to be more homogeneous, leading to denser and more regular beads. Previous studies on macromolecule diffusion and adsorption, as well as volume reduction during maturation between Ca^{2+} and Cu^{2+}-crosslinked beads, support this hypothesis [19,28]. Moreover, the symmetry around each cation should be considered, as it can also influence the structure and texture of the final beads.

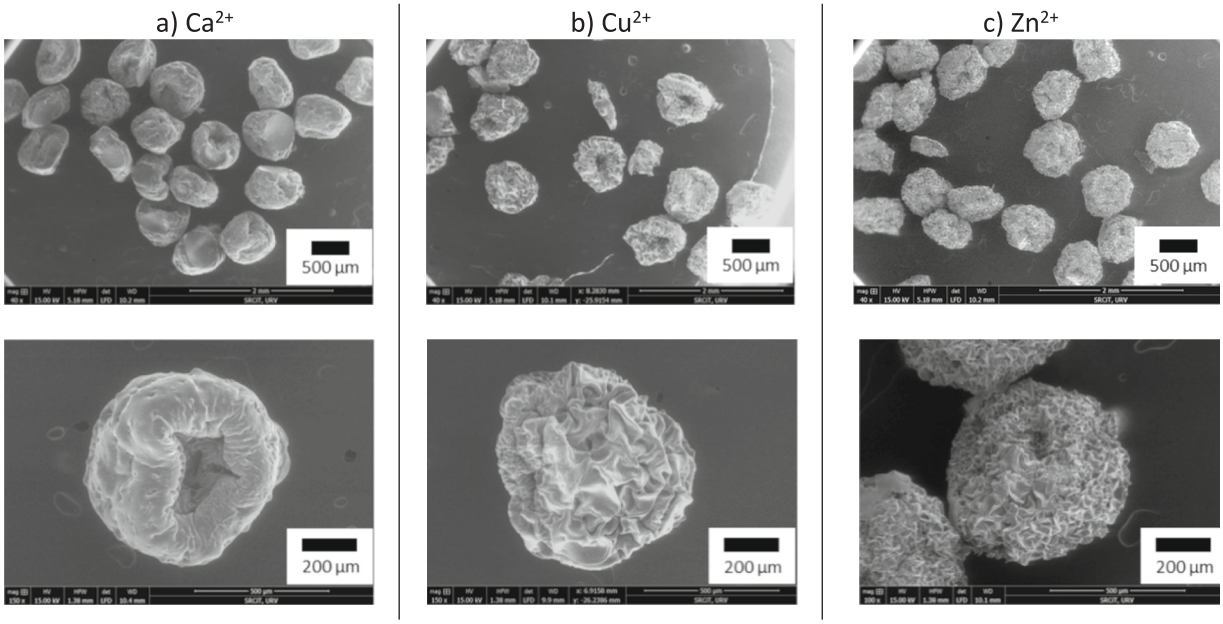

Fig. 5. ESEM micrographies of alginate beads crosslinked with 0.5 wt%: (a) $CaCl_2$; (b) $CuCl_2$; (c) $ZnCl_2$, submitted to 48 h maturation and dried at 40 °C 24 h. Top: general view; Bottom: detail of a single bead.

To explore the beads homogeneity and get insight into their formation mechanism, beads were withdrawn from the crosslinking bath containing 0.5 wt% XCl_2 at different maturation times, cryofractured and their cross-sections were observed by ESEM. The corresponding micrographies are reported in Fig. 6.

The comparison of the micrographies taken at different times shows different evidences several notable findings:

- Changes in beads' internal morphology were observed in all investigated systems up to 48 h, which confirms that this time period is necessary to reach a steady-state gel. No morphological variations were found beyond this time.

- Although the cross-section of calcium-based beads after 48 h was not clearly observable, it was evident that, at this maturation time, copper and zinc-based beads exhibited a less dense core structure compared to calcium beads. These observations are in agreement with the proposed crosslinking mechanism.

When the cation concentration in the crosslinking bath was increased, two factors should be considered: 1) the outer wall was expected to have more crosslinking points, resulting in increased rigidity and reduced permeability, potentially preventing homogeneous growth of the inner gel; 2) the cation concentration difference between the crosslinking bath and the interior of the bead was higher, favoring cation diffusion toward the center of the bead. Hence, the balance between these opposing factors was responsible for the final morphology.

Regarding the beads obtained by adding alginate to 2 wt% XCl_2, the corresponding micrographies are shown in Figs. S4 and S5.

Fig. S4 shows the same trend found in 0.5 wt%, regarding the outer surface of the beads after 48 h maturation: calcium beads (a) exhibited the smoothest surface, while copper beads (b) had increasingly rougher surface and, even more, in zinc beads (c). Concerning the internal morphology and its evolution over time (Fig. S5), the images suggest that there was no significant difference in the case of calcium beads (a) with respect to the previous case. Differently, copper beads (b) appear internally denser, growing in a "spongy" manner, while zinc beads (c) still exhibit a considerable lack of material in the center. This suggests that, in the case of copper, cation diffusion prevails over the wall rigidity, while in the case of zinc, the opposite occurs, and the formation of a more rigid wall is expected. This difference is also reflected in the beads' mechanical properties, as it will be shown further in Section 3.4.

Analyzing the images of the surface in the 10 wt% XCl_2 systems (Fig. S6) it is evidenced that calcium beads (a) still exhibit a very smooth surface, while copper beads (b) show a highly irregular surface. This is reasonably expected when we consider that in the latter case acidic gelation could be predominant, though ionotropic gelation cannot be completely ruled out. Surprisingly, at 10 wt% concentration, zinc beads display a very smooth surface, which suggests that in this case the cation diffusion through the outer wall is higher due to the concentration difference. Indeed, Fig. S7 demonstrates that while Zn-based beads still have an empty core after one hour, the internal morphology evolves into a multi-layer, denser structure over time. Nevertheless, the coexistence

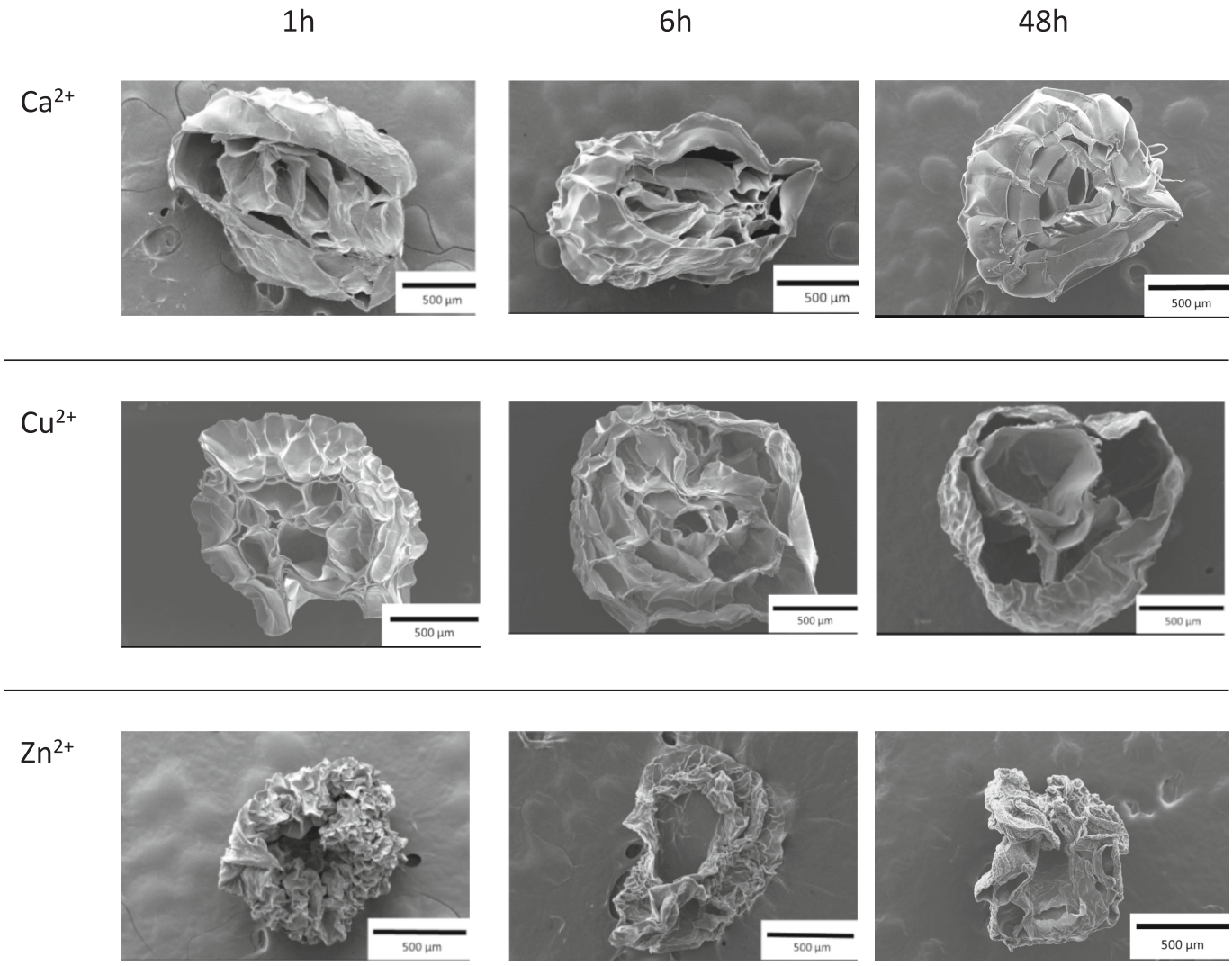

Fig. 6. FESEM micrographies of the cross-sections of alginate beads crosslinked with 0.5 wt% $CaCl_2$, $CuCl_2$, $ZnCl_2$, after 1, 6 and 48 h maturation.

of denser and more empty regions still holds after 48 h, giving rise to an irregular inner morphology. A multi-layer morphology can be found also in Ca and Cu-based beads, though they appear to contain more polymer, which is more homogeneously distributed.

3.4. Mechanical characterization

All the systems under investigation were mechanically characterized in compression mode after drying at 40 °C for 24 h. The corresponding values of Young Modulus (E) and Strength at break (σ_b) are shown in Fig. 7. The fracture images of the beads can be observed in Fig. 9. The discussion of these results needs to take into account two factors: 1) the composition of the material, which determines the number of cross-linking points in the gel as well as the strength of the bonds formed; 2) the bead morphology, which affects the strength of the outer wall and the crack propagation under compression.

When one considers the beads obtained at XCl_2 0.5 wt%, it is clearly evident that the Ca-based system is less rigid and resistant (Fig. 7). For calcium-alginate systems, rheological behavior has demonstrated that most part of the crosslinks are not permanent, but move or break under shearing [54]; indeed, optical micrographies of mechanically tested samples (Fig. 9) demonstrate that the beads flatten out rather than break under the applied stress, with a clear elastoplastic behavior, as also visible from the load-displacement curves reported in Fig. 8. This is also in line with the image of the final inner morphology of Fig. 6, which shows the presence of a compact core with many planes that contribute to stand the compression stress. On the other hand, better mechanical

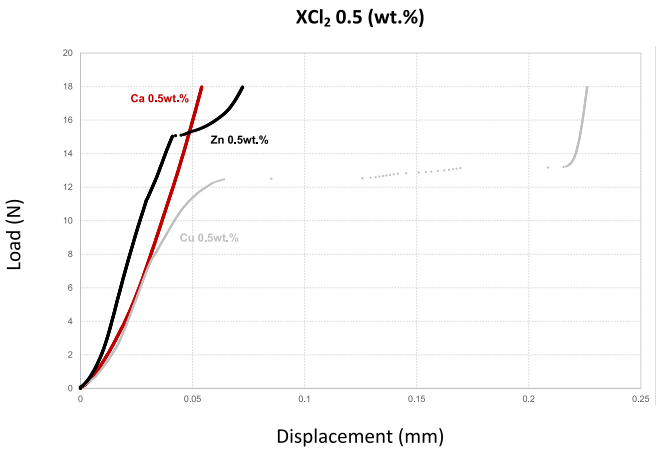

Fig. 8. Load-displacement curves for the compression tests for beads prepared with XCl_2 0.5 wt%. Red curve refers to beads prepared with $CaCl_2$, grey curve refers to beads prepared with $CuCl_2$ and black curve to $ZnCl_2$.

properties were found for Cu- and Zn-based systems. This can be interpreted on the presence of stronger and directional coordination bonds between the alginate units and the cations. Both systems exhibit a relatively empty core: therefore, their mechanical resistance is mainly due to the outer layer. The inner morphology shown by FESEM (Fig. 6) suggests the presence of a thicker outer shell in the case of Zn-based

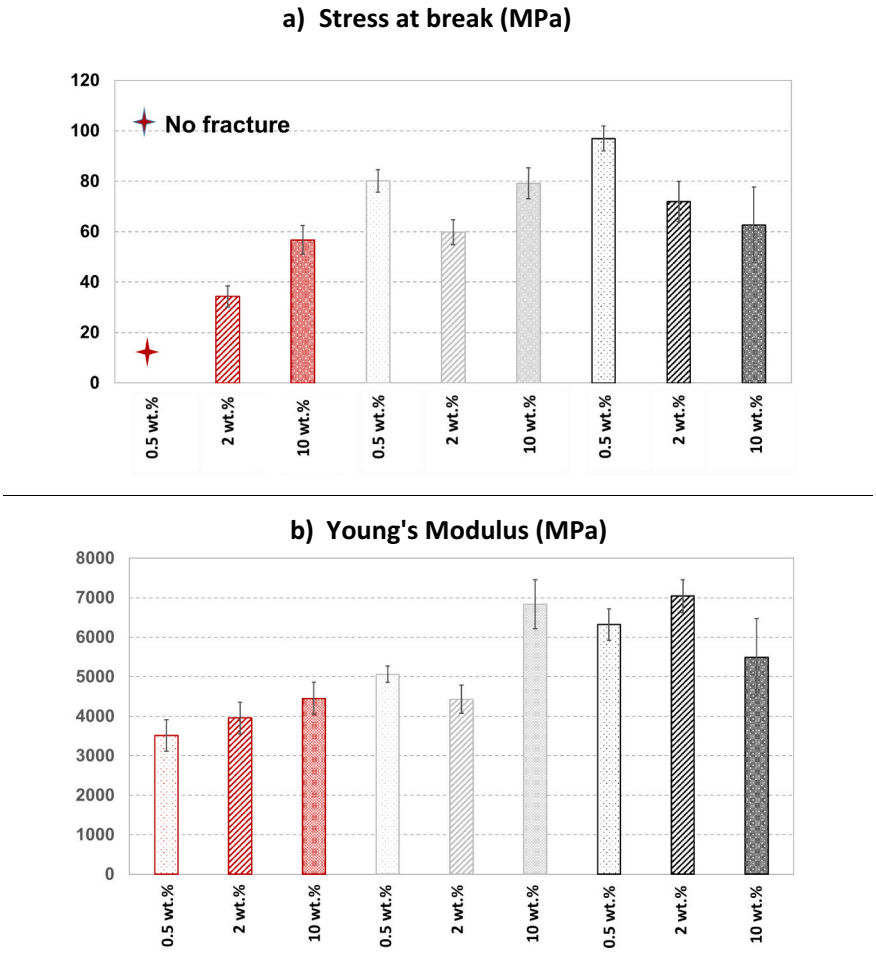

Fig. 7. (a) Strength at break (σ_b) and (b) Young Modulus (E) of M-alginate beads obtained at different XCl_2 concentrations after 48 h maturation and drying at 40 °C for 24 h. Red bars refer to beads prepared with $CaCl_2$, grey bars refer to $CuCl_2$ and black bars to $ZnCl_2$.

beads, which could justify their highest E and σ_b values. Indeed, while a complete failure was found in the case of copper beads, cracks could be evidenced in zinc ones (Fig. 9). Load-displacement curves clearly reflected the difference in the fracture mechanism of these systems (Fig. 8).

Considering the beads obtained by XCl_2 2 %, we can see, in the case of Ca, higher values of Young's modulus and differences in the mechanical strength (Fig. 7). This can be reasonably expected since higher concentration of cation determines more crosslinking points in the gel. This increase in the rigidity is reflected in the fracture behavior, with small cracks appearing before failure and in the load-displacement curve (Figs. 9 and S8, respectively); indeed, the change in the slope in the curve is evidence of the appearance of these small cracks, although still maintaining some elastoplastic behavior. The inner structure of the beads appeared similar to the 0.5 % ones (Fig. S5), as previously discussed, which helps flattening of the bead rather than a complete failure. As regarding the copper-based beads, they exhibit a more ductile behavior with less strength (Fig. 7). It should be also considered that, at the determined pH for this coagulation bath, a hybrid system could be formed, in which around 20 % U units exist in the acidic form and are not complexed with the cation. The beads' core appeared fuller than 0.5 % (Fig. S5) and this is in agreement with the micrography of fractured samples (Fig. 9) and the load-displacement curve (Fig. S8). The fracture of the 2 % samples exhibited small cracks while maintaining the mechanical integrity; in addition, a slight change in the slope in their load-displacement curve (Fig. S8) was observed, indicative of a more ductile behavior than Cu 0.5 wt% samples. In the case of zinc-based beads, they resulted more rigid and less deformable than 0.5 %, with lower strength (Fig. 7), probably due to the thinner outer wall; the images of tested samples showed that they totally break into different parts (Fig. 9), which is coherent with the empty core-shell structures evidenced in Fig. S5 and the load-displacement curve (Fig. S8).

Finally, when the beads from XCl_2 10 % were mechanically tested, the following evidences were found. As for Ca, the load-displacement behavior was found similar to 2 wt% samples (Fig. S9) with slightly higher Young's Modulus and strength, thanks to the higher number of crosslinking points. The load-displacement curve, with the change in the slope at higher loads, evidenced the appearance of cracks at higher values of strength than in the 2 wt% curve. The images of the fractured samples showed again that a considerable flattening of the beads occurred before crack starting, in agreement with FESEM images of cross-section (Fig. S7); nevertheless, in this case the cracks resulted more evident (Fig. 9) in agreement with higher rigidity and less ductile behavior. On the other hand, the beads obtained out of 10 % copper chloride exhibited significant higher rigidity than the 2 % ones (Fig. 7), with load-displacement curves very different to 2 % samples, though similar to 0.5 wt% ones, thus revealing a more fragile mechanical behavior (Fig. S9). This is in line with the quite regular and compact inner structure evidenced by FESEM in this case (Fig. S7). Nevertheless, it is important to point out that in this case a hybrid gel, alginic acid + copper alginate, whose mechanical properties are not easily predicted, was surely formed; on the other hand, the images of fractured samples (Fig. 9) agree with a more compact and homogeneous inner structure. Zn-based beads evidenced a remarkably different behavior: in this case, the values of mechanical properties resulted more scattered (Fig. 7), thus suggesting internal inhomogeneity, which was confirmed by FESEM images of beads cross-section (Fig. S7). Indeed, in Zn-based beads, fuller regions coexist with more empty ones and the outer shell can have very different thicknesses: hence, the mechanical behavior strongly depended on the contact region where the compression test was performed. That is the main reason for the lowest mean value of strength but with a very high deviation. The fracture images of the broken samples showed in Fig. 9 also evidenced scattered results, with some samples completely broken in several parts and others broken in two parts. The same

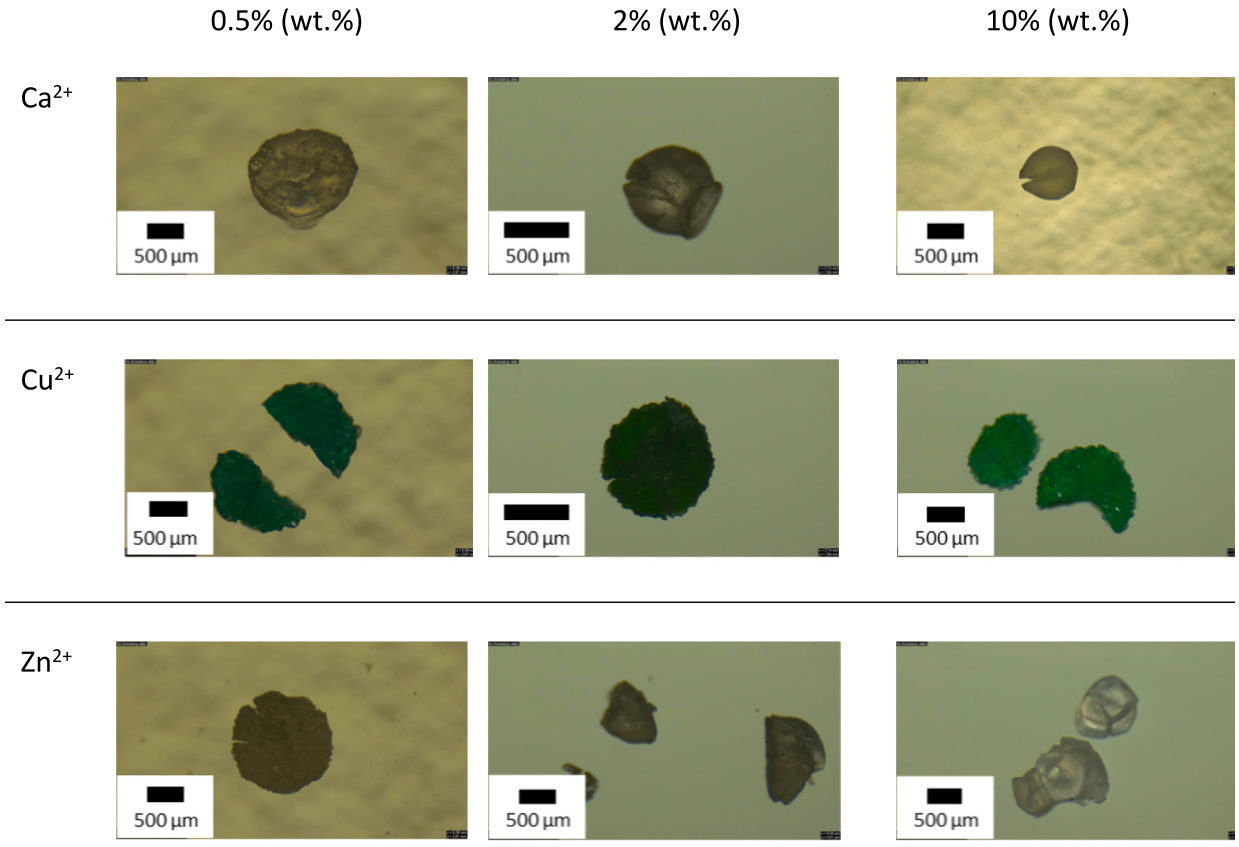

Fig. 9. Images taken from the broken/failure samples after the compression test.

comments applied to the Young's Modulus, slightly lower in mean value than 0.5 % and 2 %, but with higher deviation.

3.5. Composition of xerogels

Thermogravimetric analysis in air was used to estimate the number of uronate per cation, as well as the water content of the metal/alginate beads. As a matter of example, Fig. S10 shows the thermogram of alginate/M^{2+} beads obtained at 0.5 wt% XCl_2 concentration. Samples were first hold isothermally at 30 °C for 15 min. In general, three regions of weight loss could be distinguished: the first one, from 30 °C to 163–195 °C, depending on the cation used, was related to the water evaporation from the beads; the second and the third ones comprise the organic part decomposition and the oxide formation, respectively, which are probably partially merged. Of course, the second region could also include partial evaporation of residual water.

Calcination in oxidizing environment gave rise exclusively to the formation of the corresponding metal oxides, as it was also confirmed by XRD analysis (Fig. S11). From the residual mass at 800 °C the oxide content and the corresponding metal amount could be calculated, as reported by Agulhon et al. [65]. On the other hand, one should remember that, in general, the calculations of the number of uronate units, imply the subtraction of the water content in the xerogel beads, which cannot be established rigorously. Therefore, the number of uronate units per cation ($n_{U/X}$) and the number of water molecules per cation ($n_{W/X}$) for the systems under investigation reported in Table 2 should be considered a simple estimation.

In the case of calcium-crosslinked systems, for the lowest cation amount ($CaCl_2$ 0.5 wt%), 2 uronate units per cation are found in the obtained beads, as calculated from TGA. On the other hand, when Ca^{2+} amount increases, $n_{U/X}$ decreases. Agulhon et al. demonstrated by computational methods that the interaction between uronate units and alkaline earth is purely electrostatic, while in the case of transition metals strong covalent-coordination bonds are established [52]. Analyses on protein crystal structures and ab initio calculations performed by Katz et al. showed that the coordination number of Ca^{2+} in crystal structures preferably range between 6 and 8; oxygen represents the most common ligand, through interaction with carboxylic groups in unidentate or bidentate manner, and at least one water molecule, depending on the coordination number [66]. On the other hand, in the case of mannuronate dimers, the structures obtained by DFT-based calculations showed that two Ca^{2+}-O distances correspond to water's oxygen and that the presence of water does not significantly alter the Ca^{2+}-O distances with respect to the water-free structures [52]. Therefore, the variation in $n_{U/X}$ and $n_{W/X}$ at different Ca^{2+} amounts could correspond to changes both in the alginate denticity and in the water molecules surrounding the cation.

In the case of Cu^{2+}, when copper chloride initial concentration is 0.5 or 2 wt%, $n_{U/X}$ is equal to 2, that corresponds to the expected theoretical value for total complexation with divalent cations; this number turns higher than 2 in the presence of cation excess. It is important to remember that, for 10 % copper chloride content in the crosslinking bath, acidic precipitation is predominantly expected because of the pH value in the crosslinking bath (Table 2). Therefore, the Cu^{2+} amount determined in this case could at least partially correspond to uncoordinated cations, which are "trapped" into the acidic gel during the precipitation. Regarding Zn^{2+}, $n_{U/X}$ was found equal to 2 for all the investigated cation concentrations, thus suggesting a homogeneous alginate coordination to this cation, regardless of its total amount.

In order to gain insight into the beads' structure, SAXS and EXAFS analyses were performed.

3.6. SAXS analysis

Fig. 10. shows the SAXS patterns in logarithmic scale for the three cations studied for 0.5, 2 and 10 % metal loading.

All patterns showed a linear slope of −4 (corresponding with a power law of q^{-4}) due to the presence of large and compact structures with smooth surfaces [67]. This effect could be attributed to the packing of the polysaccharides when the gel is dry to consolidate the xerogel bead. However, low metal loadings (0.5 %) showed also the reminiscence of the rod-like structure previously described for gels [65]; this kind of structures were observed even for less explored cations such as Ce^{3+} [68]. The rod like contribution was obtained from the fitting procedure and it was plotted as a dashed line in Fig. 10. A shift in these contribution to the lower angles means an increase in the structure size. Thus Ca^{2+} xerogels showed smaller rod diameter than Cu^{2+} or Zn^{2+}; however, the d spacing obtained from the Bragg peak position at q range between 1 and 2 nm^{-1} had an opposite trend. Fitting results of the investigated samples at 0.5 % can be found in Table 3. The Bragg peak was the only correlation contribution observed, Wide Angle X-Ray Scattering patterns were also measured where the samples were mainly amorphous and only a subtle long spacing correlation could be observed. As a matter of example, Fig. S12 depicts the WAXS pattern of Zn-alginate pulverized beads obtained at 0.5 wt% $ZnCl_2$.

The rod-like structure diameter followed the same order of magnitude for X^{2+}-Alginate hydrogels and aerogels reported by other authors [65]. However, in the present case, the Ca^{2+} xerogels showed a lower

Table 3
Structural parameters obtained from SAXS pattern fittings for XCl_2 0.5 wt% samples and dry bead diameter as measured by digital Thickness Gage. The rod-like structure diameter is calculated by Diameter = $2\sqrt{2}$ Rg.

Cation XCl_2 0.5 %	Rod Rg (nm)	Rod diameter (nm)	$d_{spacing}$ (nm) Bragg peak	Q_{rod} / Q_{dp}	Bead diameter (mm)
Ca^{2+}	3.10 ± 0.01	8.77 ± 0.03	4.49	8.65	0.47 ± 0.03
Cu^{2+}	3.37 ± 0.01	9.53 ± 0.03	4.27	6.66	0.44 ± 0.01
Zn^{2+}	4.24 ± 0.03	11.99+ ± 0.09	3.85	5.92	0.42 ± 0.01

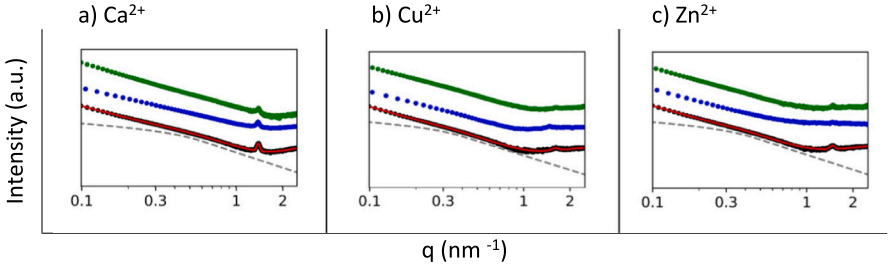

Fig. 10. SAXS patterns expressed in loglog scale for X-alginate xerogels where X: a) Ca^{2+}, b) Cu^{2+} and c) Zn^{2+}. In each panel, from the bottom to the top: 0.5 (red), 2 (blue) and 10 wt% (green) sample, respectively. The continuous line is the fitting results for 0.5 % of loading while the dashed line represents the rod-like structure contribution to the total intensity.

diameter than Cu^{2+}.

The Q_{rod} / Q_{dp} relationship computed in Table 3 quantifies the arbitrary scale relationship between the rod-like structure quantity regarding the densely packing domains one by the calculation of the invariant Q [67] and taking account the rod-like function and the Gaussian contribution invariant of the diffraction peak [69]:

$$Q_{rod} \Big/ Q_{dp} = \frac{C_1 \int_0^\infty P_{GP}(q, Rg) q2dq}{C_2 \int_0^\infty G(q, qc_1, FWHM_1) q2dq} \quad (10)$$

The decrease of the Q_{rod} / Q_{dp} parameter means an increase in the average amount of densely packed nanodomains with respect to the remaining rods. It is interesting to note that this increase can be associated to lower capsule size (Table 3), probably as a consequence of a more compact structure at microscopic level.

Interestingly, on increasing the metal chloride concentration in the bath to 2 or 10 % (Fig. 9), the rod-like structure features were almost lost or at least the contribution of the compacted region hid the remained "isolated" rods intensity since the large particles scatter more than small ones [67]. Indeed, the diffraction peak position could be glimpsed in those samples; however, there was no clear tendency of the peak intensity with concentration. Nevertheless, this evidence suggested that only in the analyzed xerogels obtained at the lowest cation concentration, a portion of the pristine gel kept somewhat preserved structure. Thus, the increase of cation concentration promoted the formation of compact structures on aging. However, the gel consolidation, aging and drying depends on several factors such as ionic strength or the charge of the polysaccharides, which depends on the pH of the media. Therefore, the rationalization of the phenomena in these complex systems is a difficult task.

3.7. Extended X-ray Absorption Fine Structure (EXAFS)

The coordination environment of Cu- and Zn-based gels was investigated by EXAFS analysis.

X-Ray Absorption Near Edge (XANES) Spectras are shown in Fig. S13 where the characteristic and the shape remain despite the metal concentration; hence, a similar local environment is expected although the metal loading concentration. However the white line (strong peak near the absorption edge) for Cu 10 % samples is less intense than the 0.5 % due to saturation effects in the detector. Thus, only 0.5 % concentration samples were employed for EXAFS analysis.

Fig. 11 shows the FFT obtained from EXAFS spectra in radial distribution for Cu, Zn 0.5 % obtained from the interval 3–14 $Å^{-1}$ K space. The transformed patterns suggested no oxide particles were formed during aging nor precipitation of the $ZnCl_2$ or $CuCl_2$ precursors. These XO particles could be excluded by the absence of a secondary contribution of Zn—Zn or Cu—Cu distances in the FFT, in both the samples after synthesis and their halogen salts. The features corresponded with organic environments linked by X-O bonds since the position of the main peak were similar to the acetate references. Since the local environment is not well known, oxygen atoms were considered as the first neighbors around metallic cations; moreover, in order to minimize the number of possible fitting parameters and avoid the overfitting, only one or two different oxygen paths were considered conforming the first shell, in accordance with the models proposed by Agulhon et al. [52]. Therefore, a single X-O path to fit the first shell using the Cu formate dihydrate was employed and two paths from Zinc oxalate. The starting guess were obtained from the LARCH database. For Cu^{2+} samples, a single path was used for the first coordination shell where the coordination number was 4.3 ± 0.4 (Bond length of 1.960 ± 0.003 Å) with Debye-Waller factor of 6×10^{-3}. Indeed, according to DFT-based calculations on MM dimers, the coordination number for Cu^{2+} complex is expected to be 4, with a bond distance ranging between 1.987 and 2.190 Å [52]. For Zn there were two distinctive oxygen bonds where the coordination number was 4.0 ± 0.2 and Zn—O bond length of 2.051 ± 0.006 Å (Debye-Waller factor of 7×10^{-3}) and a second path with a coordination number of 1.1 ± 0.1 with 2.34 ± 0.02 Å Zn—O bond length but a larger Debye Waller factor of 0.01. The latter path seems to indicate the presence of a labile water molecule in the Zn^{2+} coordination sphere. This could suggest that,

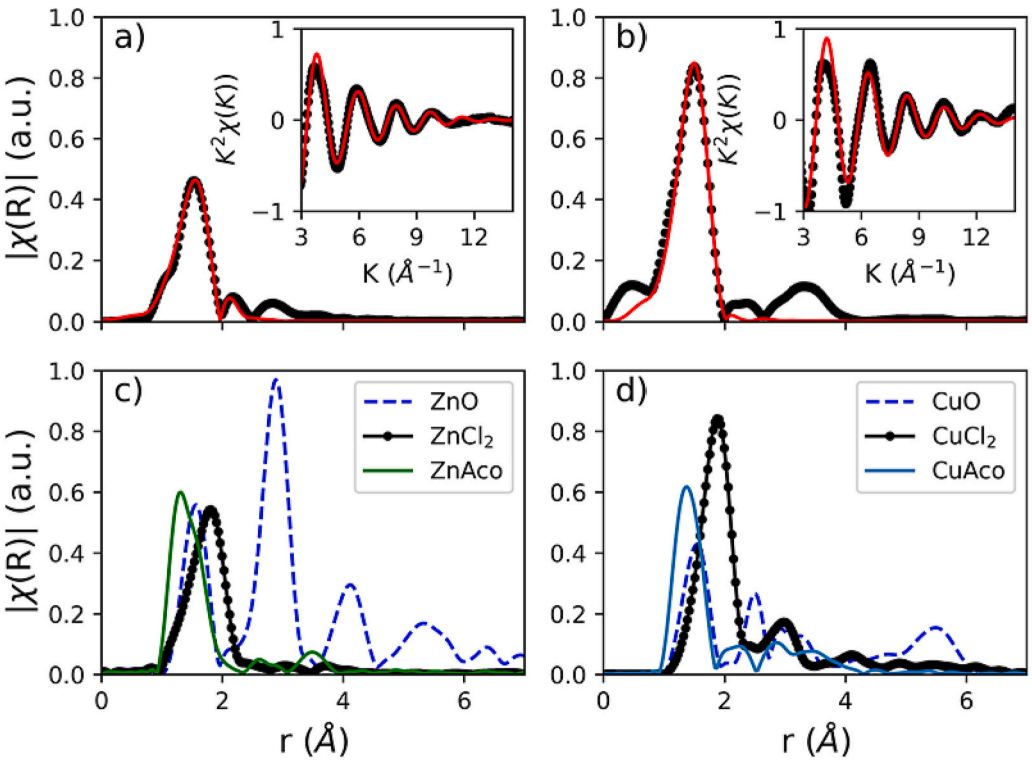

Fig. 11. Fourier transform of the EXAFS spectra for Zn (a) and Cu (b) samples loaded with 0.5 % of metal. References are also plotted for comparative analysis c) ZnO, $ZnCl_2$ and Zn^{2+} acetate (ZnAco). d) CuO, $CuCl_2$ and Cu^{2+} acetate (CuAco).

in the alginate beads obtained at 0.5 % cation chloride concentration in the bath, each Zn^{2+} could be coordinating 4 oxygens from uronate moieties and one water molecule. The fitting obtained under this hypothesis gave quite good results, as shown in Fig. 11. Indeed, the coordination number of Zn^{2+}, as determined by Agulhon et al.s calculations [52], was determined as 5.

3.8. FT-IR analysis

As previously mentioned in Section 3.3, FT-IR spectroscopy can be used to get information about the metal-carboxylate interactions in the complex with alginate [55,61,70,71]. In fact, it was found that the separation between the asymmetric and symmetric vibrational modes of carboxylate groups in the metal complex can be correlated to changes in the CO bond length and the OCO angle [72]; therefore, the separation of these bands gives rise to the following interpretation [73]: $\Delta\nu(COO^-)_{complex} < <\Delta\nu(COO^-)_{Na}$ corresponds to bidentate chelating coordination; $\Delta\nu(COO^-)_{complex} \sim \Delta\nu(COO^-)_{Na}$ corresponds to bidentate bridging coordination; $\Delta\nu(COO^-)_{complex} > > \Delta\nu(COO^-)_{Na}$ corresponds to unidentate coordination. The FT-IR spectra between 600 and 4000 cm^{-1} of Na-alginate and X-alginate beads obtained from XCl_2 0.5 wt% after 48 h maturation time are shown in Fig. 3, while the zoom of these spectra between 700 and 1750 cm^{-1} is reported in Fig. S14. The following qualitative evidence can be pointed out from Fig. S14: in agreement with the NMR characterization, the band corresponding to mannuronate residues (812–814 cm^{-1}) was evident in all the samples, while the one assigned to guluronate residues (around 730 cm^{-1}) could not be evidenced at all, thus confirming the predominance of M units in the studied alginate; the band at 1080 cm^{-1}, assigned to the C-OH stretching vibration is evident and sharper in sodium alginate, while it appears much broader and smaller in the other samples, suggesting that the hydroxilic oxygen participates in the coordination with the divalent cations [74,75]. As for the $\Delta\nu(COO^-)_{complex}$ values of the XCl_2 0.5 wt% beads after 48 h' maturation (Table 1), they all range between 150 and 180 cm^{-1} while $\Delta\nu(COO^-)_{Na}$ for the sodium alginate under investigation resulted 190 cm^{-1} According to some authors [55], this difference suggests a "pseudo-bridged" unidentate arrangement, where one carboxylic oxygen interacts with the cation, while the other forms a hydrogen bond with an adjacent hydroxyl group. On the other hand, this arrangement was proposed for the polyguluronate-metal complex, according to the "egg-box" model; in our case, the presence of M-rich alginate could give rise to a different arrangement, making the determined $\Delta\nu(COO^-)_{complex}$ value compatible with a bidentate bridging coordination [55]. Therefore, considering the calculated number of uronate per cation (Table 2), FT-IR and EXAFS results, for the 0.5 % $CuCl_2$ and $ZnCl_2$ xerogels beads we can make the hypothesis of one divalent cation surrounded by 4 C—O, each pertaining to a different carboxylic group; in this way, the cation would work as a tetrafunctional "crosslinking agent" for M-rich alginate (Fig. S15); eventually, additional coordination positions could be occupied by either hydroxylic groups from the alginate, or from water molecules. This situation could hold also for higher concentrations in the case of Zn, while the hybrid precipitation which occurs in the case of Cu, makes its coordination harder to predict.

4. Conclusions

Mannuronic-rich alginate xerogel beads crosslinked with Ca, Cu or Zn cations at different concentrations were prepared and characterized in terms of morphology, composition assessment, mechanical properties and interactions between U and the different cations. The optimization of xerogels preparation procedure was proposed by increasing the maturation time up to 48 h on the basis of microscopic observation and FT-IR experiments. This extended maturation time allowed the formation of novel, compact alginate/X^{2+} structures, with novel characteristics. In case of crosslinking with Ca^{2+} and Zn^{2+} almost exclusively ionotropic gelation was considered as a mechanism of beads formation, whereas in case of Cu^{2+} beads a hybrid formation process involving both ionotropic gelation along with acid precipitation was proposed. Scanning Electron Microscopy showed very different surfaces as well as internal structures among the cryofractured beads based on different cations. These findings reveal the different crosslinking mechanisms, which depend on the rigidity and permeability of the bead wall and the cation concentration in the bath. Interestingly, Zn-based beads exhibited a well-defined core-shell structure, which enhances their potential for future applications.

Mechanical characterization of the different beads combined with ESEM and optical microscopic observations demonstrated that in general Cu- and Zn-based systems exhibited better mechanical properties compared to Ca-based system. This outcome can be reasonably expected due the presence of stronger and directional coordination bonds between the alginate units and the transition metals employed. On the other hand, Ca-based beads exhibited an elastoplastic behavior and high ductility, which progressively decreased on increasing the metal concentration and therefore the number of crosslinking points.

The composition of alginate/X^{2+} structures was investigated. Notably, the number of Uronate units per ion of Zn^{2+} was estimated as equal to 2 and remained constant within the range of Zn^{2+} concentrations studied, indicating homogeneous coordination of uronate moieties with this cation. For Cu^{2+} the combination of ionotropic and acidic gelation elevated the number of Uronate units per ion to 2.3. Regarding the diverse compositions of Ca beads, the differences might be associated to changes both in the alginate denticity and in the water molecules surrounding the cation.

SAXS analysis revealed that pristine gel rod-like structure was only detected in beads obtained at lower cation concentrations.

The coordination environment of Cu and Zn gels was investigated by EXAFS for the 0.5 % XCl_2 xerogels. It is noteworthy that the coordination number for Cu^{2+} samples was 4.3 ± 0.4, while each Zn^{2+} ion could be coordinating 4 oxygens from U moieties and one water molecule. This evidence is in agreement with the reported Density Functional Calculations (DFT) results on Cu^{2+} – and Zn^{2+}-dimannuronate complexes. Based on FT-IR analyses, EXAFS data and beads' composition results, a hypothesis of bridging coordination was proposed for these cation-alginate systems.

From an applicative point of view, these results demonstrate that Zn can be used as an effective crosslinking agent for high-M alginates, leading to beads with good mechanical properties and a core-shell structure, which is highly desirable for microencapsulation of active agents. Therefore, given the beneficial anti-oxidant, emulsifying, biocompatible and non-mitogenic properties of high-M alginates, this cation-alginate combination results promising, for instance, for clinical applications.

We can foresee that future research efforts will be directed toward different goals, including a better understanding of the influence of factors such as crosslinker type and concentration on the performance of the final M-rich beads as active agent providers, etc. Additionally, the comparison between the characteristics of M-rich and G-rich alginate beads is fundamental. All these efforts should be devoted to the design of particles for specific, controlled and tailored applications in the food, pharmaceutical, and biomedical industry.

Declaration of competing interest

The authors declare no conflict of interest.

Data availability

Data will be made available on request.

Acknowledgements

The authors are grateful to Universitat Rovira i Virgili for financial support of Ms. Reig-Vano's scholarship (2019PMF-PIPF-20) and for financing through 2022PFR-URV-05. This work is also part of the R&D project PID2020-115102RB-C21 funded by MCNI/AEI/10.13039/501100011033. Thanks to Núria Argany Figueras, Dra. Rita Marimon Picó, Mercè Moncusí Mercadé and Dra. Mariana Stefanova Stankova of Servei de Recursos Científic i Tècnic (SRCiT-URV) for their patience and full assistance in microscopy experiments.

Appendix A. Supplementary data

Supplementary data to this article can be found online at https://doi.org/10.1016/j.ijbiomac.2023.125659.

References

[1] A. Gonzalez-Pujana, G. Orive, J. Pedraz, E. Santos Vizcaíno, R. Hernandez, Alginate Microcapsules for Drug Delivery, 2018, pp. 67–100, https://doi.org/10.1007/978-981-10-6910-9_3.
[2] A. Sosnik, Alginate particles as platform for drug delivery by the oral route: state-of-the-art, ISRN Pharm. 2014 (2014), 926157, https://doi.org/10.1155/2014/926157.
[3] K. Lee, D. Mooney, Alginate: properties and biomedical applications, Prog. Polym. Sci. 37 (2012) 106–126, https://doi.org/10.1016/j.progpolymsci.2011.06.003.
[4] M. Lopes, B. Vieira, F. Veiga, R. Seiça, L. Cabral, P. Arnaud, J. Andrade, A. Ribeiro, Preparation methods and applications behind alginate-based particles, Expert Opin. Drug Deliv. 5247 (2016) 1–14, https://doi.org/10.1080/17425247.2016.1214564.
[5] J. Patil, P. Gurav, S. Marapur, A. Banagar, Ionotropic Gelation and Polyelectrolyte Complexation Technique: Novel approach for Drug Encapsulation, 2015, p. 271.
[6] Y. Yang, O.H. Campanella, B.R. Hamaker, G. Zhang, Z. Gu, Rheological investigation of alginate chain interactions induced by concentrating calcium cations, Food Hydrocoll. 30 (1) (2013) 26–32, https://doi.org/10.1016/j.foodhyd.2012.04.006.
[7] J. Kozlowska, W. Prus, N. Stachowiak, Microparticles based on natural and synthetic polymers for cosmetic applications, Int. J. Biol. Macromol. 129 (2019) 952–956, https://doi.org/10.1016/j.ijbiomac.2019.02.091.
[8] S.H. Ching, N. Bansal, B. Bhandari, Alginate gel particles–a review of production techniques and physical properties, Crit. Rev. Food Sci. Nutr. 57 (6) (2017) 1133–1152, https://doi.org/10.1080/10408398.2014.965773.
[9] R. Theagarajan, S. Dutta, J.A. Moses, A. Chinnaswamy, Alginates for Food Packaging Applications, 2019, pp. 205–232, https://doi.org/10.1002/9781119487999.ch11.
[10] M. Szekalska, A. Puciłowska, E. Szymańska, P. Ciosek, K. Winnicka, Alginate: current use and future perspectives in pharmaceutical and biomedical applications, Int. J. Polym. Sci. 2016 (2016) 7697031, https://doi.org/10.1155/2016/7697031.
[11] B. Reig-Vano, B. Tylkowski, X. Montané, M. Giamberini, Alginate-based hydrogels for cancer therapy and research, Int. J. Biol. Macromol. 170 (2021) 424–436, https://doi.org/10.1016/j.ijbiomac.2020.12.161.
[12] N.T.T. Uyen, Z.A.A. Hamid, N.X.T. Tram, N. Ahmad, Fabrication of alginate microspheres for drug delivery: a review, Int. J. Biol. Macromol. 153 (2020) 1035–1046, https://doi.org/10.1016/j.ijbiomac.2019.10.233.
[13] M.G. Funaro, K.V. Nemani, Z. Chen, Z.M. Bhujwalla, K.E. Griswold, B. Gimi, Effect of alginate microencapsulation on the catalytic efficiency and in vitro enzyme-prodrug therapeutic efficacy of cytosine deaminase and of recombinant E. coli expressing cytosine deaminase, J. Microencapsul. 33 (1) (2016) 64–70, https://doi.org/10.3109/02652048.2015.1115902.
[14] T. Andersen, P. Auk-Emblem, M. Dornish, 3D cell culture in alginate hydrogels, Microarrays 4 (2) (2015) 133–161, https://doi.org/10.3390/microarrays4020133.
[15] D. Dhamecha, R. Movsas, U. Sano, J.U. Menon, Applications of alginate microspheres in therapeutics delivery and cell culture: past, present and future, Int. J. Pharm. 569 (2019), 118627, https://doi.org/10.1016/j.ijpharm.2019.118627.
[16] R. Dorati, I. Genta, M. Ferrari, G. Vigone, V. Merico, S. Garagna, M. Zuccotti, B. Conti, Formulation and stability evaluation of 3D alginate beads potentially useful for cumulus–oocyte complexes culture, J. Microencapsul. 33 (2) (2016) 137–145, https://doi.org/10.3109/02652048.2015.1134691.
[17] S.N. Pawar, K.J. Edgar, Alginate derivatization: a review of chemistry, properties and applications, Biomaterials 33 (11) (2012) 3279–3305, https://doi.org/10.1016/j.biomaterials.2012.01.007.
[18] J. Rodrigues, R. Lagoa, Copper ions binding in cu-alginate gelation, J. Carbohydr. Chem. 25 (2006) 219, https://doi.org/10.1080/07328300600732956.
[19] C.-Y. Yu, H. Wei, Q. Zhang, X.-Z. Zhang, S.-X. Cheng, R.-X. Zhuo, Effect of ions on the aggregation behavior of natural polymer alginate, J. Phys. Chem. B 113 (45) (2009) 14839–14843, https://doi.org/10.1021/jp906899j.
[20] G. Klöck, A. Pfeffermann, C. Ryser, P. Gröhn, B. Kuttler, H.-J. Hahn, U. Zimmermann, Biocompatibility of mannuronic acid-rich alginates, Biomaterials 18 (10) (1997) 707–713, https://doi.org/10.1016/S0142-9612(96)00204-9.
[21] W. Jiao, W. Chen, Y. Mei, Y. Yun, B. Wang, Q. Zhong, H. Chen, W. Chen, Effects of molecular weight and guluronic acid/mannuronic acid ratio on the rheological behavior and stabilizing property of sodium alginate, Molecules 24 (23) (2019) 4374.
[22] M. Şen, Effects of molecular weight and ratio of guluronic acid to mannuronic acid on the antioxidant properties of sodium alginate fractions prepared by radiation-induced degradation, Appl. Radiat. Isot. 69 (1) (2011) 126–129, https://doi.org/10.1016/j.apradiso.2010.08.017.
[23] A. Kadir, M.T.M. Mokhtar, T.W. Wong, Nanoparticulate assembly of Mannuronic acid- and guluronic acid-rich alginate: oral insulin carrier and glucose binder, J. Pharm. Sci. 102 (12) (2013) 4353–4363, https://doi.org/10.1002/jps.23742.
[24] T.A. Davis, F. Llanes, B. Volesky, A. Mucci, Metal selectivity of Sargassum spp. and their alginates in relation to their alpha-L-guluronic acid content and conformation, Environ. Sci. Technol. 37 (2) (2003) 261–267.
[25] I.D. Hay, Z. Ur Rehman, A. Ghafoor, B.H.A. Rehm, Bacterial biosynthesis of alginates, J. Chem. Technol. Biotechnol. (1986) 85 (6) (2010) 752–759, https://doi.org/10.1002/jctb.2372.
[26] E.D.T. Atkins, I.A. Nieduszynski, W. Mackie, K.D. Parker, E.E. Smolko, Structural components of alginic acid. II. The crystalline structure of poly-α-L-guluronic acid. Results of X-ray diffraction and polarized infrared studies, Biopolymers 12 (8) (1973) 1879–1887, https://doi.org/10.1002/bip.1973.360120814.
[27] Y. Cao, H. Cong, B. Yu, Y. Shen, A review on the synthesis and development of alginate hydrogels for wound therapy, J. Mater. Chem. B 11 (13) (2023) 2801–2829, https://doi.org/10.1039/d2tb02808e.
[28] A. Łętocha, M. Miastkowska, E. Sikora, Preparation and characteristics of alginate microparticles for food, pharmaceutical and cosmetic applications, Polymers 14 (18) (2022) 3834–3866. https://doi.org/10.3390/polym14183834.
[29] C. Ouwerx, N. Velings, M. Mestdagh, M.A. Axelos, Physico-chemical properties and rheology of alginate gel beads formed with various divalent cations, Polym. Gels Netw. 6 (5) (1998) 393–408.
[30] B. Salvati, P. Santagapita, M. Perullini, Exploring the conditions to generate alginate nanogels, J. Sol-Gel Sci. Technol. 102 (1) (2022) 142–150, https://doi.org/10.1007/s10971-021-05631-w.
[31] N.M. Velings, M.M. Mestdagh, Physico-chemical properties of alginate gel beads, Polym. Gels Netw. 3 (3) (1995) 311–330, https://doi.org/10.1016/0966-7822(94)00043-7.
[32] N. Veronica, P.W.S. Heng, C.V. Liew, Alginate-based matrix tablets for drug delivery, Expert Opin. Drug Deliv. 20 (1) (2023) 115–130, https://doi.org/10.1080/17425247.2023.2158183.
[33] A.S. Prasad, Biochemistry of Zinc, Biochemistry of the Elements Series vol. 11, Springer, New York, NY, 2013.
[34] H. Cheng, H. Wu, T. Guo, H. Jin Park, J. Li, Zinc insulin hexamer loaded alginate zinc hydrogel: preparation, characterization and in vivo hypoglycemic ability, Eur. J. Pharm. Biopharm. 179 (2022) 173–181, https://doi.org/10.1016/j.ejpb.2022.08.016.
[35] E.A. Günter, O.V. Popeyko, Delivery system for grape seed extract based on biodegradable pectin-Zn-alginate gel particles, Int. J. Biol. Macromol. 219 (2022) 1021–1033, https://doi.org/10.1016/j.ijbiomac.2022.08.040.
[36] Z. Zheng, J. Qi, L. Hu, D. Ouyang, H. Wang, Q. Sun, L. Lin, L. You, B. Tang, A cannabidiol-containing alginate based hydrogel as novel multifunctional wound dressing for promoting wound healing, Biomater. Adv. 134 (2022), 112560, https://doi.org/10.1016/j.msec.2021.112560.
[37] K. Aiedeh, M. Taha, Y. Al-Hiari, Y. Bustanji, H. Alkhatib, Effect of ionic crosslinking on the drug release properties of chitosan diacetate matrices, J. Pharm. Sci. 96 (2007) 38–43, https://doi.org/10.1002/jps.20764.
[38] N. Raut, P. Deshmukh, M. Umekar, N. Kotagale, Zinc cross-linked hydroxamated alginates for pulsed drug release, Int. J. Pharm. Investig. 3 (2013) 194–202, https://doi.org/10.4103/2230-973x.121292.
[39] W. Klinkajon, P. Supaphol, Novel copper (II) alginate hydrogels and their potential for use as anti-bacterial wound dressings, Biomed. Mater. 9 (2014), 045008, https://doi.org/10.1088/1748-6041/9/4/045008.
[40] M. Vinceković, N. Jalšenjak, S. Topolovec-Pintarić, E. Đermić, M. Bujan, S. Jurić, Encapsulation of biological and chemical agents for plant nutrition and protection: chitosan/alginate microcapsules loaded with copper cations and Trichoderma viride, J. Agric. Food Chem. 64 (43) (2016) 8073–8083, https://doi.org/10.1021/acs.jafc.6b02879.
[41] T.T. Le, K. Murugesan, C.-S. Lee, C.H. Vu, Y.-S. Chang, J.-R. Jeon, Degradation of synthetic pollutants in real wastewater using laccase encapsulated in core–shell magnetic copper alginate beads, Bioresour. Technol. 216 (2016) 203–210, https://doi.org/10.1016/j.biortech.2016.05.077.
[42] H. Hertz, Ueber die Berührung fester elastischer Körper 1882 (92) (1882) 156–171, https://doi.org/10.1515/crll.1882.92.156.
[43] K. Kim, J. Cheng, Q. Liu, X.Y. Wu, Y. Sun, Investigation of mechanical properties of soft hydrogel microcapsules in relation to protein delivery using a MEMS force sensor, J. Biomed. Mater. Res. A 92A (1) (2010) 103–113, https://doi.org/10.1002/jbm.a.32338.
[44] C.X. Wang, C. Cowen, Z. Zhang, C.R. Thomas, High-speed compression of single alginate microspheres, Chem. Eng. Sci. 60 (2005) 6649–6657.
[45] G. Ashiotis, A. Deschildre, Z. Nawaz, J.P. Wright, D. Karkoulis, F.E. Picca, J. Kieffer, The fast azimuthal integration Python library: pyFAI, J. Appl. Crystallogr. 48 (2015) 510–519, https://doi.org/10.1107/S1600576715004306.
[46] A. Posbeyikian, E. Tubert, A. Bacigalupe, M.M. Escobar, P.R. Santagapita, G. Amodeo, M. Perullini, Evaluation of calcium alginate bead formation kinetics: an integrated analysis through light microscopy, rheology and microstructural SAXS, Carbohydr. Polym. 269 (2021), 118293, https://doi.org/10.1016/j.carbpol.2021.118293 (Epub 2021 Jun 3).
[47] B. Hammouda, A new Guinier–Porod model, J. Appl. Crystallogr. 43 (2010), https://doi.org/10.1107/s0021889810015773.

[48] I. Zazzali, T.R. Aguirre Calvo, V.M. Pizones Ruíz-Henestrosa, P.R. Santagapita, M. Perullini, Effects of pH, extrusion tip size and storage protocol on the structural properties of Ca(II)-alginate beads, Carbohydr. Polym. 206 (2019) 749–756, https://doi.org/10.1016/j.carbpol.2018.11.051.
[49] G.T. Grant, E.R. Morris, D.A. Rees, P.J.C. Smith, D. Thom, Biological interactions between polysaccharides and divalent cations: the egg-box model, FEBS Lett. 32 (1) (1973) 195–198, https://doi.org/10.1016/0014-5793(73)80770-7.
[50] W. Mackie, S. Perez, R. Rizzo, F. Taravel, M. Vignon, Aspects of the conformation of polyguluronate in the solid state and in solution, Int. J. Biol. Macromol. 5 (6) (1983) 329–341, https://doi.org/10.1016/0141-8130(83)90056-9.
[51] C.A. Steginsky, J.M. Beale, H.G. Floss, R.M. Mayer, Structural determination of alginic acid and the effects of calcium binding as determined by high-field n.m.r, Carbohydr. Res. 225 (1) (1992) 11–26, https://doi.org/10.1016/0008-6215(92)80036-Z.
[52] P. Agulhon, V.K. Markova, M. Robitzer, F. Quignard, T. Mineva, Structure of alginate gels: interaction of diuronate units with divalent cations from density functional calculations, Biomacromolecules 13 (6) (2012) 1899–1907, https://doi.org/10.1021/bm300420z.
[53] H. Kaygusuz, G.A. Evingür, Ö. Pekcan, R. von Klitzing, F.B. Erim, Surfactant and metal ion effects on the mechanical properties of alginate hydrogels, Int. J. Biol. Macromol. 92 (2016) 220–224.
[54] M. Mancini, M. Moresi, R. Rancini, Mechanical properties of alginate gels: empirical characterisation, J. Food Eng. 39 (4) (1999) 369–378, https://doi.org/10.1016/S0260-8774(99)00022-9.
[55] S.K. Papageorgiou, E.P. Kouvelos, E.P. Favvas, A.A. Sapalidis, G.E. Romanos, F. K. Katsaros, Metal–carboxylate interactions in metal–alginate complexes studied with FTIR spectroscopy, Carbohydr. Res. 345 (4) (2010) 469–473.
[56] Z. Belattmania, S. Kaidi, S. El Atouani, C. Katif, F. Bentiss, C. Jama, A. Reani, B. Sabour, V. Vasconcelos, Isolation and FTIR-ATR and 1H NMR characterization of alginates from the main alginophyte species of the Atlantic coast of Morocco, Molecules 25 (18) (2020) 4335, https://doi.org/10.3390/molecules25184335.
[57] H.M. Jensen, F.H. Larsen, S.B. Engelsen, Characterization of alginates by nuclear magnetic resonance (NMR) and vibrational spectroscopy (IR, NIR, Raman) in combination with chemometrics, in: D.B. Stengel, S. Connan (Eds.), Natural Products from Marine Algae: Methods and Protocols, Springer, New York, New York, NY, 2015, pp. 347–363, https://doi.org/10.1007/978-1-4939-2684-8_22.
[58] H. Grasdalen, B. Larsen, O. Smidsrød, A p.m.r. study of the composition and sequence of uronate residues in alginates, Carbohydr. Res. 68 (1) (1979) 23–31, https://doi.org/10.1016/S0008-6215(00)84051-3.
[59] P.E. Ramos, P. Silva, M.M. Alario, L.M. Pastrana, J.A. Teixeira, M.A. Cerqueira, A. A. Vicente, Effect of alginate molecular weight and M/G ratio in beads properties foreseeing the protection of probiotics, Food Hydrocoll. 77 (2018) 8–16, https://doi.org/10.1016/j.foodhyd.2017.08.031.
[60] T. Ramdhan, S.H. Ching, S. Prakash, B. Bhandari, Time dependent gelling properties of cuboid alginate gels made by external gelation method: effects of alginate-CaCl2 solution ratios and pH, Food Hydrocoll. 90 (2019) 232–240, https://doi.org/10.1016/j.foodhyd.2018.12.022.
[61] C. Sartori, D.S. Finch, B. Ralph, K. Gilding, Determination of the cation content of alginate thin films by FTi.r. spectroscopy, Polymer 38 (1) (1997) 43–51, https://doi.org/10.1016/S0032-3861(96)00458-2.
[62] F. Burriel-Martí, F. Lucena-Conde, S. Arribas-Jimeno, J. Hernández-Méndez, Química Analítica Cualitativa, Ediciones Paraninfo, 2002.
[63] A. Haug, Dissociation of alginic acid, Acta Chem. Scand. 15 (4) (1961) 950–952.
[64] S. Chaberek, A.E. Martell, Organic Sequestering Agents, Wiley, New York, 1959.
[65] P. Agulhon, M. Robitzer, L. David, F. Quignard, Structural regime identification in ionotropic alginate gels: influence of the cation nature and alginate structure, Biomacromolecules 13 (1) (2012) 215–220, https://doi.org/10.1021/bm201477g.
[66] A.K. Katz, J.P. Glusker, S.A. Beebe, C.W. Bock, Calcium ion coordination: a comparison with that of beryllium, magnesium, and zinc, J. Am. Chem. Soc. 118 (24) (1996) 5752–5763, https://doi.org/10.1021/ja953943i.
[67] A.F. Craievich, Small-angle X-ray scattering by nanostructured materials, in: L. Klein, M. Aparicio, A. Jitianu (Eds.), Handbook of Sol-Gel Science and Technology, Springer International Publishing, Cham, 2016, pp. 1–46, https://doi.org/10.1007/978-3-319-19454-7_37-1.
[68] J. Sonego, P. Santagapita, M. Perullini, M. Jobbagy, Ca(II) and Ce(III) homogeneous alginate hydrogels from parent alginic acid precursor: a structural study, Dalton Trans. 45 (2016), https://doi.org/10.1039/c6dt00321d.
[69] N. Torasso, A. Vergara-Rubio, P. Rivas-Rojas, C. Huck-Iriart, A. Larrañaga, A. Fernández-Cirelli, S. Cerveny, S. Goyanes, Enhancing arsenic adsorption via excellent dispersion of iron oxide nanoparticles inside poly(vinyl alcohol) nanofibers, J. Environ. Chem. Eng. 9 (1) (2021), 104664, https://doi.org/10.1016/j.jece.2020.104664.
[70] J.P. Chen, L. Hong, S. Wu, L. Wang, Elucidation of interactions between metal ions and ca alginate-based ion-exchange resin by spectroscopic analysis and modeling simulation, Langmuir 18 (24) (2002) 9413–9421, https://doi.org/10.1021/la026060v.
[71] T. Dudev, C. Lim, The effect of metal binding on the characteristic infrared band intensities of ligands of biological interest, J. Mol. Struct. 1009 (2012) 83–88, https://doi.org/10.1016/j.molstruc.2011.09.007.
[72] M. Nara, H. Torii, M. Tasumi, Correlation between the vibrational frequencies of the carboxylate group and the types of its coordination to a metal ion: an ab initio molecular orbital study, J. Phys. Chem. 100 (51) (1996) 19812–19817, https://doi.org/10.1021/jp9615924.
[73] K. Nakamoto, Infrared and Raman Spectra of Inorganic and Coordination Compounds, Handbook of Vibrational Spectroscopy, John Wiley & Sons, Ltd, 2006.
[74] Y. Liu, J. Zhao, C. Zhang, H. Ji, P. Zhu, The flame retardancy, thermal properties, and degradation mechanism of zinc alginate films, J. Macromol. Sci. B 53 (6) (2014) 1074–1089, https://doi.org/10.1080/00222348.2014.891169.
[75] X. Zhang, L. Wang, L. Weng, B. Deng, Strontium ion substituted alginate-based hydrogel fibers and its coordination binding model, J. Appl. Polym. Sci. 137 (16) (2020) 48571, https://doi.org/10.1002/app.48571.